Research Paper

Metamorphism and exhumation of basement gneiss domes in the Quadrilátero Ferrífero: Two stage dome-and-keel evolution?

Kathryn Cutts [a,*], Cristiano Lana [a], Fernando Alkmim [a], Federico Farina [a,b], Hugo Moreira [a,c], Viviane Coelho [a]

[a] Applied Isotope Research Group, Departamento de Geologia, Escola de Minas, Universidade Federal de Ouro Preto, Morro do Cruzeiro, 35400-000, Ouro Preto, MG, Brazil
[b] Department of Earth Sciences, University of Geneva, Rue des Maraîchers 13, 1205, Geneva, Switzerland
[c] School of Earth and Environmental Sciences, University of Portsmouth, Burnaby Building, Burnaby Road, Portsmouth, PO1 3QL, UK

A R T I C L E   I N F O

A B S T R A C T

The presence of dome-and-keel provinces in Archean cratons has been connected with the initiation of plate tectonics on Earth as these features are most commonly observed in Archean rocks. The Quadrilátero Ferrífero in Brazil has been identified as a Paleoproterozoic dome-and-keel province for more than three decades. The prevailing model suggests that it formed during the Rhyacian Transamazonian orogeny, making it unique among dome-and-keel provinces. However, a lack of appropriate lithologies, datable minerals and the metamorphic overprint of later orogenesis has resulted in a cryptic metamorphic record for the formation of this dome-and-keel province. A clinopyroxene-bearing migmatite from the core of the Bação dome has peak $P-T$ conditions of 5−7 kbar and 700−750 °C and a published age of ca. 2730 Ma based on U−Pb ages of zircon from leucosomes, suggesting that this age represents the migmatisation event. A fine-grained epidote-albite-titanite assemblage overprints the coarse-grained clinopyroxene and amphibole, giving $P-T$ conditions of 8−9 kbar and 550 °C with an associated titanite age of ca. 2050 Ma. A garnet-bearing amphibolite sample also from the core of the dome has peak $P-T$ conditions of 7−8 kbar and 650−700 °C, and texturally late titanite from this sample produces an age of ca. 2060 Ma. Three additional samples were collected from the edges of the dome. A garnet-gedrite bearing felsic schist produces peak $P-T$ conditions of 8−9 kbar and 650−700 °C on a clockwise $P-T$ evolution. This sample has a U−Pb zircon age of ca. 2775 Ma, which could date metamorphism or be the age of its volcaniclastic protolith. Texturally unconstrained titanite from the sample gives an age of ca. 2040 Ma. A garnet-bearing amphibolite that occurs as a boudin within the felsic schist gives both zircon and titanite ages of ca. 2050 Ma and has peak $P-T$ conditions of 5−6 kbar and 650−700 °C on a near isobaric $P-T$ path. An amphibolite dike, observed to cross-cut the felsic schist produces a zircon U−Pb age of ca. 2760 Ma. Altogether this data suggests that the samples were metamorphosed in the Archean (ca. 2775−2730 Ma) and again during the Transamazonian event. The most plausible explanation for this data is that dome-and-keel formation occurred in the Archean with migmatisation and high-temperature metamorphism occurring at this time. The Paleoproterozoic event is interpreted as a reactivation of the dome-and-keel formation structures, with Paleoproterozoic keels crosscutting Archean keels and producing metamorphic aureoles. The high radiogenic heat production and the presence of dense sedimentary successions in Archean terranes make dome-and-keel provinces a uniquely Archean feature, but they are susceptible to reworking, resulting in an enigmatic record of formation.

1. Introduction

The ongoing debate on the initiation of plate tectonics on Earth (Davies, 1992; Hamilton, 1998; Stern, 2005; Brown, 2006, 2007a,

* Corresponding author.
E-mail address: kathryn.cutts@gmail.com (K. Cutts).

2007b; Condie and Pease, 2008; Brown, 2010; Van Hunen and Moyen, 2012; Gerya, 2014) is very closely associated with the presence of dome-and-keel geometries in many Archean cratons (Van Kranendonk et al., 2004, 2007; Lana et al., 2010a; François et al., 2014; Van Kranendonk et al., 2014; Sizova et al., 2015). The distinctive geometric pattern of the dome-and-keel provinces is unrelated to recognizable regional, structural or metamorphic trends, but seems to reflect an enigmatic deviation from conventional strains of extensional/compressional tectonics. This may reflect the weakness of ancient felsic crust as a result of high radiogenic thermal output and mafic underplating, and be largely unrelated to Archean plate tectonic processes (Bédard et al., 2013). Alternatively, some workers have proposed that the geometric pattern was formed because conventional plate tectonics was not operating in the Archean but rather the nature of Archean felsic rocks acted as a driver for an entirely different process, with the formation of dome-and-keel provinces being the result of gravitationally driven, vertical tectonic processes (Collins, 1989; Van Kranendonk et al., 2004, 2007, 2014). This does not necessarily mean that horizontal tectonic processes were not operating simultaneously (e.g. Lin, 2005; Lin et al., 2013).

Two fundamentally distinct classes of dome-and-keel provinces are recognized (Marshak et al., 1997): M-type provinces (M for magmatic), in which the domes represent granitoid plutons intruding a pre-existing supracrustal rock assemblage; and B-type provinces (B for basement), in which the domes are made up essentially of gneisses and granitoids significantly older than the supracrustal assemblage. The intrusion of younger granitoids into older or similar age sediments present no major questions for the development of the M-type architectures, such as those displayed by the Canadian Abitibi belt (Mueller et al., 1996; Chown et al., 2002) and the Australian Eastern Gold Fields Superterrane of the Yilgarn Craton (Morris and Witt, 1997; Nelson, 1997; Chen et al., 2004). However, the formation processes of the B-type dome-

and-keel provinces (e.g., the Barberton Greenstone belt and the East Pilbara Terrane of the Pilbara Craton, although both these regions also experienced later M-type doming), remain inconclusive and are still a matter of debate in the literature (Kisters et al., 2003; Van Kranendonk et al., 2007, 2014; Cutts et al., 2014, 2015; Brown et al., 2015; Nijman et al., 2017).

Several models try to explain the formation of the enigmatic B-type dome-and-keel structures. These include: 1) the aforementioned gravitationally driven, partial convective overturn (Anhaeusser et al., 1969; Hickman, 1984; Collins, 1989; Williams and Collins, 1990; Hippertt, 1994; Sandiford et al., 2004; Van Kranendonk et al., 2004, 2007); 2) superimposed folding creating regional dome-and-keel interference patterns (Drake and Morgan, 1980; Dimroth et al., 1983; Myers and Watkins, 1985; Hudleston et al., 1988); and 3) up-warping or steepening of a regional extensional detachment, i.e. a metamorphic core complex (Bickle et al., 1980, 1985; Chemale et al., 1994; Kisters et al., 2003; Lana et al., 2010b).

The Quadrilátero Ferrífero (QF) mining district in the southern São Francisco craton of Brazil hosts a B-type dome-and-keel province. The basement consists of ca. 3200−2800 Ma granitoid-gneiss complexes and the keels are composed of 2900−2100 Ma supracrustal sequences. Dome formation is interpreted to have occurred at ca. 2050 Ma (Marshak et al., 1997; Alkmim and Marshak, 1998). This age determination is based on the depositional age of the youngest supracrustal sequence occurring in the keels at ca. 2125 Ma (the Sabara Group; Machado et al., 1996), as well as on a garnet-muscovite-whole rock Sm−Nd age of 2095 ± 65 Ma from the metamorphic aureole on the northern side of the Serra do Curral (Fig. 1; Marshak et al., 1997). However, several lines of evidence challenge the Paleoproterozoic formation of this dome-and-keel province: 1) the domes are mostly made up of gneisses however, poorly deformed granites are also abundant (Fig. 1). These are all Neoarchean with ages mostly spanning 2770−2700 Ma
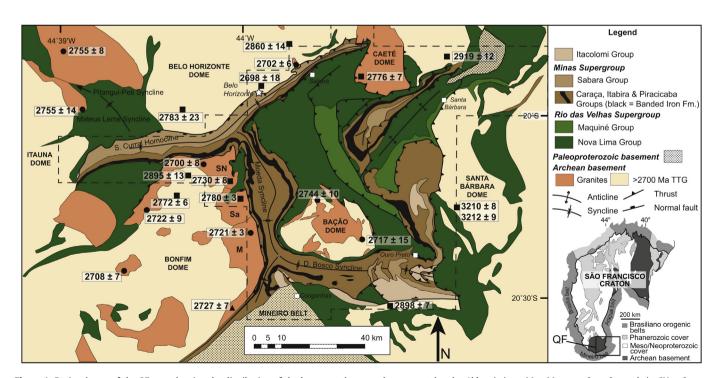
Figure 1. Regional map of the QF area showing the distribution of the basement domes and supracrustal rocks. Abbreviations: M — Mamona, Sa — Samambaia, SN — Souza-Noschese, granite plutons. The dashed black line indicates the originally defined area of the Quadrilátero Ferrífero (Dorr, 1969; Farina et al., 2016). The ages plotted on the figure are previously published U-–Pb ages (in Ma, compiled from Machado et al., 1992; Machado and Carneiro, 1992; Lana et al., 2013; Romano et al., 2013; Farina et al., 2015a) with squares indicating TTG ages, circles indicating potassic granitioid ages, and triangles being interpreted metamorphic ages.

(Machado and Carneiro, 1992; Machado et al., 1992, 1996; Teixeira et al., 1996; Lana et al., 2013; Romano et al., 2013; Farina et al., 2015a); 2) the migmatitic gneisses are also all Archean in age (Machado and Carneiro, 1992; Machado et al., 1992, 1996; Noce et al., 1998; Farina et al., 2016; Teixeira et al., 2017).

Considering that plate tectonic processes were active in the late Archean, these rocks and structures present a unique opportunity to study the processes involved in the formation of dome-and-keel provinces and to understand why they are so common in Archean terrains. A greater understanding of the formation of dome-and-keel provinces will further the debate about the onset of plate tectonic processes in terms of whether these unique structures could be the result of particular plate tectonic processes, and the nature of processes that preceded plate tectonics.

The objectives of this study are to determine whether dome-and-keel formation in the QF happened in the Archean or Paleo-proterozoic then use this information to interpret the tectonic evolution of the QF and compare to other dome-and-keel provinces. To achieve this we will investigate samples from the Bação dome complex in the central QF (Figs. 1 and 2) using a combination of U–Pb zircon and titanite geochronology and metamorphic phase equilibria. Three rock samples were obtained along the km-wide shear zones that separate the dome from the overlying supra-crustal units and two samples from within the Bação basement complex. The results of this study suggest that dome-and-keel formation in the QF initiated in the Archean with later Paleo-proterozoic reworking.

2. Regional geology

The São Francisco Craton in eastern Brazil is a large, well-exposed shield, surrounded by Neoproterozoic fold belts (Heilbron et al., 2017, Fig. 1). The basement in the northern part of the craton is separated into the Gavião, Jequié, Serrinha and Ita-buna-Salvador-Curaçá blocks. Each of these Archean to Paleo-proterozoic blocks is bounded by major ca. 2100 Ma suture zones (Teixeira and Figueiredo, 1991; Barbosa and Sabate, 2004; Aguilar et al., 2017). To the south, the craton consists of amphibolite
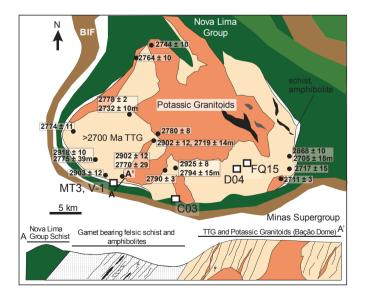

Figure 2. Sketch map of the Bação dome showing main lithologies and sample lo-calities (white squares). The black circles with ages in boxes indicate previously pub-lished U–Pb ages from the Bação dome (Lana et al., 2013; Romano et al., 2013; Farina et al., 2015a). All ages are in Ma and ages marked with an 'm' were interpreted to be metamorphic while unmarked ages are magmatic (Farina et al., 2015a).

facies granitoid gneiss complexes (e.g. Bonfim, Belo Horizonte, Bação, Santa Bárbara and Caeté) and polydeformed, low-grade Archean to Proterozoic supracrustal sequences.

The Quadrilátero Ferrífero (QF) is in the southern portion of the craton, bordered to the east by the Neoproterozoic Araçuaí Belt and to the south by the Paleoproterozoic Mineiro Belt (Fig. 1). Folds and thrusts in the region are represented by a NE-orientation in the northernmost section of the QF, whereas in the south, the regional structures are NS and E–W trending. This pattern results from the superposition of two major tectonic episodes: the Rhyacian 2100–2000 Ma Transamazonian contraction and extension, as well as the Ediacaran-Cambrian Brasiliano orogeny (Marshak et al., 1997; Alkmim and Marshak, 1998; Farina et al., 2016; Aguilar et al., 2017; Alkmim and Teixera, 2017).

The region has two major lithostratigraphic units which are arranged in a distinctive structural architecture (Chemale et al., 1994; Marshak et al., 1997; Alkmim and Marshak, 1998; Alkmim and Martins-Neto, 2012). The Archean granitoid-gneiss complexes are exposed in the core of domal structures such as the Bação, Belo Horizonte, Caeté, Santa Bárbara and Bonfim domes (Fig. 1). The domes expose three main groups of rocks: 1) fine-grained banded orthogneiss intruded by 2) leucogranites and aplitic/pegmatite veins and dikes; and by 3) medium-coarse grained, mostly weakly foliated granites.

The banded gneisses alternate between leucocratic and meso-cratic bands varying in width from 2 mm to 10 cm and define a penetrative amphibolite facies foliation. A small proportion of gneisses correspond to non-foliated migmatites (Farina et al., 2015a), showing folded sheets and pods of leucogranites.

Geochemistry indicates that the banded gneisses are medium-K and have a similar composition to Archean Tonalite-Trondhjemite-Granodiorite (TTG) series rocks (Farina et al., 2015a; Albert et al., 2016). The crystallization ages of these rocks fall into three groups named Santa Bárbara (ca. 3220–3200 Ma, only poorly preserved in the Santa Bárbara dome), Rio dos Velhas I (ca. 2930–2850 Ma) and Rio dos Velhas II (ca. 2800–2760 Ma; Lana et al., 2013). The leuco-cratic dikes, local migmatisation and age of the amphibolite facies foliation are dated at ca. 2770 Ma with many magmatic zircons that give Rio das Velhas I crystallization ages having a metamorphic rim that gives a Rio das Velhas II age (Lana et al., 2013; Farina et al., 2016). Two weakly foliated plutons (the Caeté and Samambaia plutons) also give an age of 2770 Ma (Machado and Carneiro, 1992; Machado et al., 1992; Noce et al., 2005).

The gneisses are intruded by multiple leucogranite sheets (cm to meter scale), which vary from subparallel to the gneissosity to younger felsic/pegmatitic dikes that crosscut the gneissosity (Lana et al., 2013). Granitic rocks form large batholiths (i.e. Mamona batholith; Fig. 1) as well as decimetre to meter scale domains or stocks intruded into or closely associated with the banded gneiss. The granites generally only preserve a weak foliation, often showing complex intermingling gneiss-granite structures, domains of granite intruding into the gneiss and xenoliths of banded gneiss hosted within granite. This widespread granitic magmatism occurred in the QF between 2750–2680 Ma with the emplacement of slightly to non-foliated granites as large batholiths (i.e., Mamona; Fig. 1; Romano et al., 2013) to small leucogranitic veins and dikes. Geochemically, these granites are high-K, and this event is considered to mark the stabilization of the craton (Romano et al., 2013).

The supracrustal sequences that form the keels between the Archean granitoid-gneiss dome complexes are separated into three sequences: 1) the Rio das Velhas Supergroup (ca. 2900–2730 Ma); 2) the Minas Supergroup (ca. 2600–2100 Ma); and 3) the Itacolomi Group (ca. 2100–2000 Ma). The Itacolomi Group is interpreted to post-date keel formation.

The Rio das Velhas Supergroup is divided into the Nova Lima and Maquiné Groups. The Nova Lima Group consists of massive komatiites to pillowed komatiitic basalts which are intercalated with chemical carbonaceous sediments, consistent with a submarine environment (Schrank et al., 1990). This was followed by submarine deposition of pelite, banded iron formation and subordinate chert, which are in turn capped by volcaniclastic sequences of conglomerate-greywacke, sandstone-greywacke and pelitic greywacke. Three volcaniclastic greywackes intercalated within the Nova Lima Group give ages of 2792 ± 11 Ma, 2773 ± 7 Ma and 2751 ± 9 Ma (Machado et al., 1992, 1996; Noce et al., 2005). The 2000 m thick Maquiné Group unconformably overlies the Nova Lima Group. This unit consists of clastic fluvial and marine sediments with the base of the unit considered a flysch to molasse type sequence, which becomes more quartz rich and conglomeritic toward the top (Dorr, 1969). The Maquiné Group has a unimodal source region (2780–2770 Ma) and a maximum deposition age of ca. 2730 Ma. This suggests that deposition occurred during or immediately after a mountain building event (Moreira et al., 2016).

The Minas Supergroup was deposited unconformably on top of the Rio das Velhas Supergroup and the granitoid gneiss terrain (Fig. 1). The base of the supergroup consists of alluvial sandstones, conglomerates and shales that grade upward into coastal marine pelites (Caraça Group; Dorr, 1969; Renger et al., 1995; Alkmim and Martins-Neto, 2012). U–Pb zircon data suggests that these early units were derived predominantly from erosion of TTG and potassic granites with a maximum deposition age of ca. 2600 Ma (Machado et al., 1996; Hartmann et al., 2006; Martínez Dopico et al., 2017). Following the shallow marine sediments, a major marine transgression occurred resulting in a period of chemical sediment precipitation, leading to the accumulation of the marker bed of the QF, the Lake Superior-type Cauê banded iron formation (in the Itabira Group). This was followed by stromatolite-rich carbonates, marine sandstones and pelites that also record U–Pb zircon ages consistent with a provenance from the QF basement (Piracicaba Group). The final unit of the Minas Supergroup, the Sabará Group, consists of a thick pile of turbidites, lithic conglomerates and diamictites that are chiefly derived from ca. 2100 Ma sources. This syn-orogenic deposition represents the closure of the Minas Basin and has a maximum deposition age of 2121 Ma (Dorr, 1969; Renger et al., 1995; Machado et al., 1996; Martínez Dopico et al., 2017).

The Itacolomi Group is separated from the Minas Supergroup by a regional unconformity and consists of an up to 2000 m thick pile of alluvial sediments (impure metasandstones, metaconglomerates and minor phyllites). While the Minas Supergroup is portrayed as a passive margin to syn-orogenic sequence, the Italcolomi Group is thought to be an intermontane molasse accumulated during the collapse phase of the Rhyacian orogeny (Marshak et al., 1992; Alkmim and Marshak, 1998; Alkmim and Martins-Neto, 2012). Zircon age determination from this unit by Machado et al. (1996; Pb–Pb) and Hartmann et al. (2006; U–Pb) produce different results with maximum depositional ages of ca. 2060 Ma and ca. 2140 Ma respectively.

3. Dome-and-keel formation and 2000 Ma metamorphism

As previously mentioned, the map/structural pattern of the QF (Fig. 1) is marked by keels of supracrustal cover rocks surrounding domes of Archean granitoid/gneisses. The strata in the keels are characterized by a lateral continuity over large (>100 km) distances, and their younging directions often point away from the domes. In contrast to a number of Archean dome-and-keel provinces, in which formation is commonly associated with intense plutonism in and around the domes, the keels of the QF expose supracrustal strata that are significantly younger than the gneisses and granitoids in the adjacent domes (Machado and Carneiro, 1992; Machado et al., 1992, 1996; Teixeira et al., 1996; Lana et al., 2013; Romano et al., 2013; Farina et al., 2015a). The QF keels contain the 2900–2600 Ma Rio das Velhas greenstone belt succession and the Paleoproterozoic Minas strata, for which the uppermost supracrustal unit (Machado et al., 1996) of the folded sequence pinpoints the maximum age for the doming event at ca. 2125 Ma. The contact between the supracrustals and granite-gneiss domes is described as strongly sheared with a dip away from the centers of the domes. Next to these contacts, the supracrustal assemblages are severely thinned or missing (Marshak et al., 1992). Regional constraints indicate that Minas keels appear to crosscut Rio das Velhas keels, suggesting that Paleoproterozoic dome-and-keel structures of the Quadrilátero Ferrífero partially reactivated a pre-existing Archean M-type dome-and-keel province (Marshak et al., 1997; Alkmim and Marshak, 1998). This is seen most clearly where the Serra do Curral Homocline meets the Mateus Leme Syncline (see Figs. 1 and 6 of Alkmim and Marshak, 1998). As shown in Fig. 1, most keels represent first order synclines (e.g. the Moeda, Dom Bosco, Pitangui-Peti, Mateus Leme synclines), and a large homocline (Serra do Curral homocline), some of them bounded by normal shear zones (Alkmim and Marshak, 1998).

Herz (1978) identified 1–4 km-wide metamorphic aureoles around the granitic domes with increasing pressure-temperature (*P–T*) conditions from the centers of the synclines towards the crystalline domes. The aureoles are characterized by progressive growth of biotite, garnet, staurolite, cordierite, and sillimanite. Garnet-bearing and staurolite-bearing schists were observed in the Nova Lima, the Piracicaba, and Sabará Groups. Outside of the metamorphic aureoles, the strata contain low greenschist facies assemblages with chlorite, muscovite, plagioclase and quartz (Herz, 1978). Detailed petrographic observations in a restricted area in the north-western portion of the QF (Jordt-Evangelista et al., 1992; also see Fig. 6 of Alkmim and Marshak, 1998) documented staurolite and kyanite that are progressively replaced by andalusite and cordierite towards the Belo Horizonte Dome. Temperatures close to 625 °C at pressures of around 3 kbar were estimated according to reactions involving kyanite + staurolite + quartz assemblages giving way to cordierite + sillimanite assemblages (Jordt-Evangelista et al., 1992). The metamorphism was linked to the dome exhumation and metamorphic zones were interpreted as a product of conductive heat emanating from hot, exhumed basement gneisses (Jordt-Evangelista et al., 1992; Marshak et al., 1992). Porphyroblasts of staurolite and garnet record syn-kinematic growth, and are marked by oriented inclusions that are slightly rotated with respect to the rock foliation. Some garnet porphyroblasts record sigmoidal inclusion trails that are continuous with a weakly curved foliation in the matrix and seem to preserve pressure shadows, indicating that shearing continued after syn-kinematic growth (Jordt-Evangelista et al., 1992; Marshak et al., 1992, 1997; Hippertt and Davis, 2000). Structural observations around the domes indicate a single pervasive shear foliation subparallel to, or at a low angle to bedding of the supracrustal strata adjacent to the domes. Basement-dome-up, supracrustal-rock-down sense of shear in the synclinal limbs is indicated by a number of meso- and microstructural shear sense indicators such as S–C fabrics, asymmetric conglomerate pebbles, and microfolds (Marshak et al., 1992; Chemale et al., 1994; Hippertt, 1994; Alkmim and Marshak, 1998; Hippertt and Davis, 2000). Steep, down-dip preferred orientations of metamorphic minerals in shear planes are often associated with the asymmetric indicators and are consistent with porphyroblast growth (Hippertt and Davis, 2000). Microfolds, rotated porphyroblasts and S–C fabrics are equally found in the basement dome rocks and make a set of undisputed kinematic evidence that the doming occurred in solid
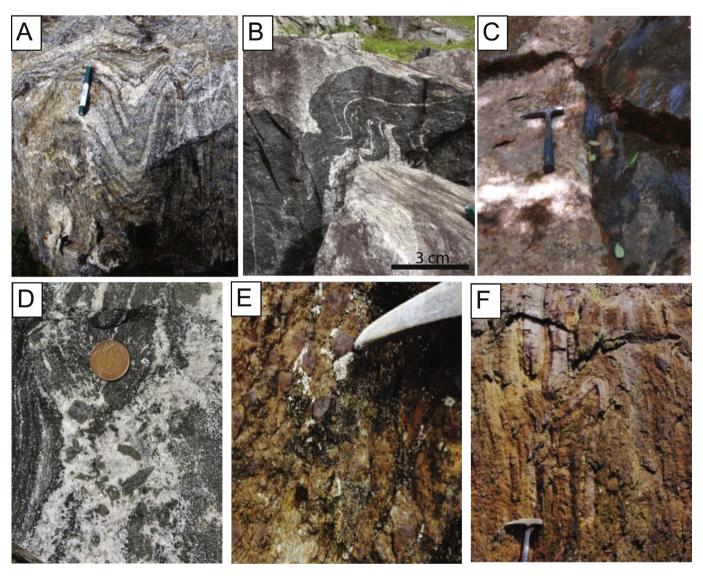
Figure 3. Field photos. (A) Banded gneisses with tightly folded melanocratic and leucocratic bands. (B) Gneisses are crosscut by metre-scale dikes. (C) Gneisses are in contact with a thin felsic schist. (D) Clinopyroxene-bearing migmatite occurring in one of the amphibolite dikes. Coin is 2 cm in diameter. (E) Garnet porphyroblasts flattened along the foliation plane. (F) Macroscopic asymmetric fold.

state, along normal shear zones under amphibolite facies conditions.

Recent monazite and titanite ages from amphibolitic and leucocratic dikes, granitoids and gneisses in the Bação, Bonfim and Belo Horizonte complexes give ages ranging between 2100−1950 Ma, suggesting that the Archean crust was affected by a long-lived metamorphic event representing the closure of the Minas Basin and the amalgamation of the Archean nuclei of the São Francisco and Congo cratons (Aguilar et al., 2017). Dome-and-keel formation is interpreted to have occurred during the extensional collapse period of this orogenic event (Marshak et al., 1997; Alkmim and Marshak, 1998).

4. The Bação complex

The Bação complex is a 20 km-diameter granitoid gneiss dome surrounded by mafic to intermediate greenschist and pelitic amphibolite facies schists (muscovite + epidote, chlorite + amphibole, staurolite) of the Nova Lima Group (Fig. 2).

The dome contains banded gneisses and migmatites around the margins and relatively homogenous granitoids in the core (Hippertt, 1994; Lana et al., 2013; Romano et al., 2013). The banded gneisses are characterized by tightly-folded biotite-rich melanocratic, and biotite-free leucocratic bands (Fig. 3A), which are vertical to subvertical and record a concentric trend parallel to the edge of the dome, reflecting the elliptical shape of the dome (e.g. Fig. 2). Large outcrops of banded gneiss are also observed in the inner part of the dome, but often show gradual transition into small, non-foliated, anatectic granites.

Geochronology on the banded gneisses indicates two age groups for crystallization, with zircon cores giving ages of ca. 2925−2900 Ma and ca. 2795 Ma (Fig. 2; Lana et al., 2013; Romano et al., 2013; Farina et al., 2015a). Zircons of the older gneisses also commonly have structureless rims which give ages of ca. 2775 Ma. Both banded gneiss and granitoids are cross-cut by numerous meter-wide amphibolite dikes that are often boudinaged and rotated into parallelism to the main gneissic banding (Fig. 3B and C). Many of these dikes have been dated at ca. 2775 Ma or are
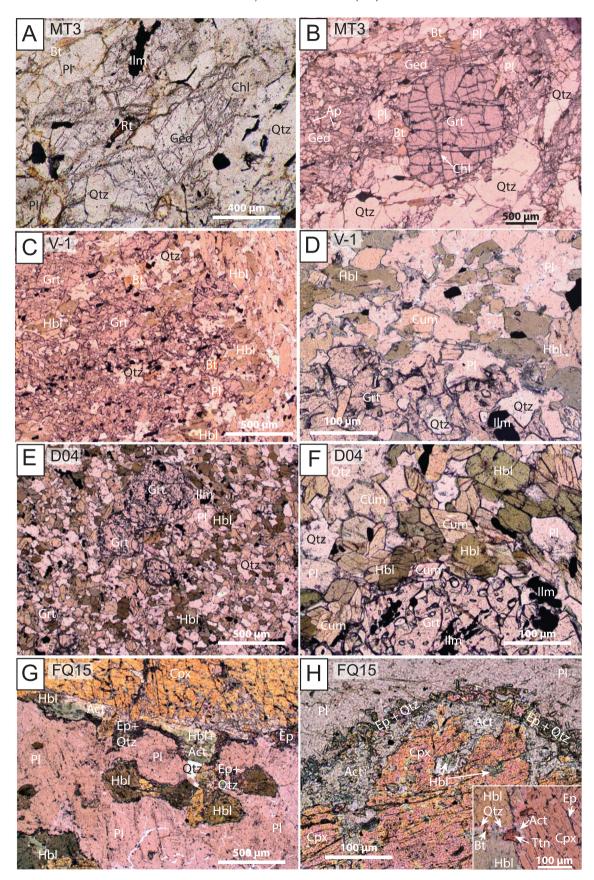
Figure 4. Photomicrographs, abbreviations from Kretz (1983). Photomicrographs showing the mineral assemblage in sample MT3 (A, B), sample V-1(C, D). sample D04 (E, F), and sample FQ15 (G, H).
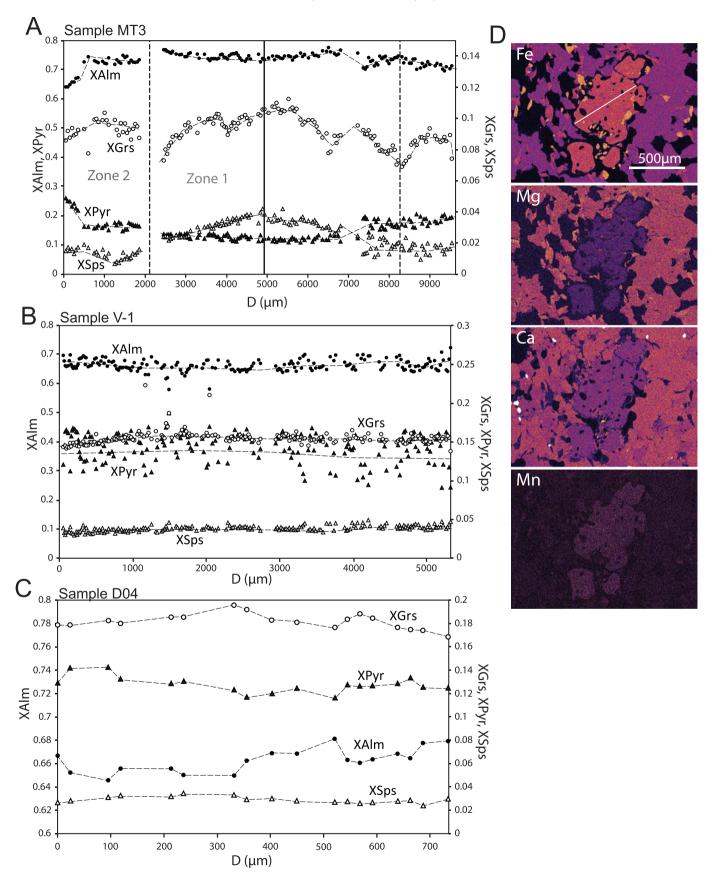
Figure 5. (A) Garnet compositional profile from sample MT3 from rim to rim of the garnet grain. (B) Garnet compositional profile from sample V-1 from rim to rim of the garnet grain. (C) Garnet compositional profile from sample D04. The location of the profile is given by the white line in Fig. 5D. (D) Elemental maps of garnet from sample D04, the white line gives the garnet compositional profile in Fig. 5C.

Sample MT3: SI(64.50)AL(14.26)TI(0.56)FE(6.42)F3(0.07) MG(8.05)MN(0.08)CA(2.15)NA(3.54)K(0.37)H(15)

Figure 6. (A) Calculated P−T pseudosection for sample MT3 based on the whole rock composition, which is given at the top of the diagram in moles. The diagram was created using the Theriak-Domino software package (De Capitani and Petrakakis, 2010)
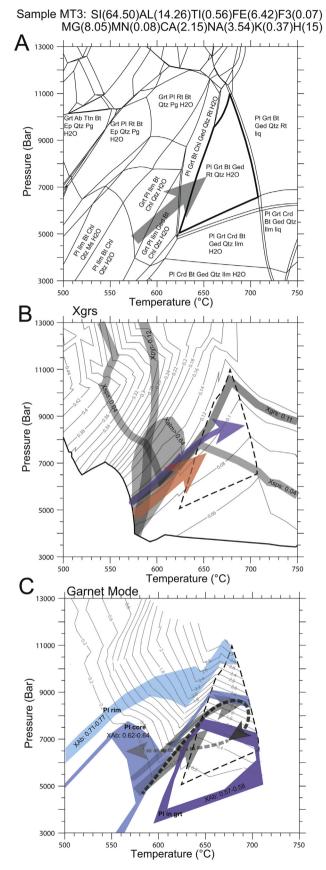
crosscut by ca. 2700 Ma granitic leucosomes (Lana et al., 2013; Romano et al., 2013; Farina et al., 2015a). Some of these dikes record amphibolite-facies metamorphic assemblages such as garnet + hornblende + plagioclase + quartz + ilmenite + titanite, with one instance showing clinopyroxene-bearing partial melting (Fig. 3D).

Two leucogranitic-pegmatite dikes in the southern part of the Bação dome yielded Paleoproterozoic U−Pb monazite ages (2030 Ma and 2022 Ma; Machado et al., 1992; Farina et al., 2016). Titanite and monazite ages from the Bação complex also give ages of ca. 2100−1940 Ma (Machado et al., 1992; Noce et al., 1998; Aguilar et al., 2017). These ages are interpreted to be due to a long-lived metamorphic event that affected the southern São Francisco Craton and the adjacent Mineiro and southern Araçuai belts (Cutts et al., 2018; Moreira et al., 2018).

The contact between the granitoid-gneisses of the dome and the Nova Lima Group is marked by a thin, discontinuous unit (Fig. 2) of biotite-gedrite-garnet felsic schist (Fig. 3C and E) which locally contains boudins of foliated, fine-grained amphibolite consisting of amphibole-biotite-epidote-garnet. The boudins are oriented parallel to the foliation but have discordant contacts indicating that they are likely intrusive into the sequence. Due to their difference in metamorphic grade and different composition, the felsic schist is not considered to be part of the Nova Lima Group but is thought to be a supracrustal rock associated with the basement complex known as the Catarina Mendes Unit (Lima da Silva, 2005). At the contact between the Catarina Mendes Unit and the basement domes the schists record a mylonitic fabric that is continuous with the mylonitic fabric in the domes. This mylonitic fabric is interpreted as part of the peripheral normal shear zones that affect the basement domes in the QF. Macroscopic asymmetric folds (Fig. 3F), rotated feldspar clasts and down-dip to oblique mineral lineation all indicate that the shearing developed during exhumation of the dome.

5. Sample locations

This study utilizes five samples from the Bação dome. Few samples are available from the QF greenstone belt that record suitable mineral assemblages for metamorphic petrology. This is mostly because of intense weathering conditions and vegetation cover in the southeastern part of Brazil. The best preserved rocks for this type of study were felsic schists and mafic rocks that were preferentially preserved around the contacts with the Bação dome and as meter-wide dikes exposed in quarries of this dome. It is worth noting however, the contacts with other basement domes expose similar rock types, but were found to be too weathered for further petrological investigation. Samples were obtained from two

with the internally consistent dataset of Holland and Powell (1998). The interpreted peak field has a bold outline, while the grey arrow indicates the P−T evolution of the sample based on the change in mineral assemblage. Mineral abbreviations as in Kretz (1983). (B) Compositional isopleths for X_{Grs} are given in grey with the black bold line indicating the garnet-in line. The grey fields are the composition of the garnet core. The bold black dashed field is the interpreted peak assemblage of the sample. The red arrow indicates the P−T evolution for the sample based on the change in mineral assemblage, whereas the blue arrow is the P−T evolution for the sample based on the change in garnet composition as well as the change in mineral assemblage. (C) Garnet mode (in mol) for sample MT3 are given in grey. The blue fields indicate the composition of plagioclase from this sample. The darkest blue field shows the X_{Ab} composition of plagioclase grains included in garnet, whereas the medium blue field shows the X_{Ab} composition of matrix plagioclase cores and the lightest blue field indicates the composition of plagioclase rims. The interpreted peak P−T assemblage field is given by the bold dashed line. The thick, dashed black arrow indicates the interpreted P−T path for this sample with the fainter section indicating less certainty. The P−T paths based on the mineral assemblage evolution and the change in garnet composition are also given in grey.

locations, the dome edge (the Catarina Mendes Unit) and the core of the dome, to see if there is any variation in $P-T$ conditions experienced throughout the dome. Samples were also selected based on their suitability for $P-T$ modeling. In particular, samples that contained garnet were targeted. The selected samples are: 1) sample MT3 is a garnet-gedrite schist collected from the Catarina Mendes Unit on the edge of the Bação dome; 2) sample V-1 is a garnet-bearing amphibolite obtained from a mafic boudin within the Catarina Mendes Unit; 3) sample CO3 is an amphibolite dike which crosscuts the Catarina Mendes Unit; 4) sample D04 is a garnet-bearing amphibolite dike from the core of the Bação dome; and 5) sample FQ15 is a migmatized amphibolite dike also from the core of the Bação dome (Fig. 2). Geochronology and phase equilibria modeling was conducted on samples MT3, V-1 and D04. Sample CO3 did not contain garnet and was only used for geochronology. Sample FQ15 has been previously dated (ca. 2066 Ma, titanite dated by Aguilar et al. (2017)) and is only used for phase equilibria modeling here.

6. Analytical methods

The petrographic study of samples MT3, D04, FQ15 and V-1 was investigated prior to the $P-T$ modeling. Petrography was carried out using a Zeiss AXIO Scope. A1 with an attached Zeiss AxioCam MRc5 to collect images.

Mineral compositional analysis was performed using a JEOL scanning electron microscope at the Universidade Federal de Ouro Preto. Textures were studied in backscattered electron (BSE) mode and phase compositions quantified by energy dispersive X-ray spectroscopy (EDS) analysis using an Oxford Instrument detector and Oxford software. Beam conditions during the quantitative analyses were 20 kV and approximately 1.5 nA, with a working distance of 13 mm and a specimen beam current of −4.0 nA. X-ray counts with the set-up used were typically 7000 cps. The counting time was 50 s live-time. Analyses were quantified using natural mineral standards, and mineral chemical compositions were recalculated to mineral stoichiometries to obtain resultant mineral structural formulae. Standards were analyzed during each analytical session and these analyses indicate that for oxides that make up more than 1 wt.% of the mineral composition, relative errors are <5%. Additionally, in each sample, typically 100−150 mineral spots were analyzed on 3−5 distinct sites, allowing for a comprehensive characterization of mineral chemistry. Fe_2O_3 is calculated for garnet, epidote and ilmenite using the method of Droop (1987). Amphibole analyses were recalculated using the Probe-Amph spreadsheet (Tindle and Webb, 1994). Representative mineral analyses from each sample are included in the supplementary information (Supplementary Appendix 1).

Pressure-temperature pseudosections were calculated for samples using the software package Theriak/Domino (De Capitani and Petrakakis, 2010) and the database of Holland and Powell (1998). The geologically realistic system MnNCKFMASHTO (MnO-Na_2O-CaO-K_2O-FeO-MgO-Al_2O_3-SiO_2-H_2O-TiO_2-Fe_2O_3) was used for sample MT3. Samples D04 and V-1 were modeled using the geologically realistic system MnNCFMASHTO (MnO-Na_2O-CaO-FeO-MgO-Al_2O_3-SiO_2-H_2O-TiO_2-Fe_2O_3). Sample FQ15 was modeled using the geologically realistic system NCKFMASHTO. The bulk composition of samples V-1, FQ15 and MT3 was determined by whole rock XRF analysis due to the presence of porphyroblasts. For sample D04, the bulk composition was obtained by calculation from the average composition of each mineral within an area, combined with the mineral proportions (e.g. Clarke et al., 2001; Kelsey, 2008). The fine grain size and layer scale compositional variability make this the best method for obtaining a phase diagram which relates to the thin-section of sample D04. The fine-grained

assemblage in sample FQ15 was also modeled using a bulk composition obtained by calculation from mineral modes and compositions within an area dominated by this assemblage. The determined composition for samples D04 and FQ15 are given in Table 1 while a phase diagram using the XRF composition for sample D04 is given in the supplementary information (Supplementary Appendix 2). K_2O was not included in the modeling for samples D04 and V-1 because it can over stabilize biotite. This occurs because the amphibole models used do not consider K_2O while amphibole grains in the sample contain up to 0.5 wt.% K_2O. Thus the modeling adds biotite to every assemblage to take up the excess K_2O.

For samples MT3, V-1 and D04, the mineral assemblages and field observations indicate peak metamorphic conditions to be sub-solidus. For this reason, H_2O was set in excess. Compositional isopleths for garnet (X_{Alm}, X_{Sps}, X_{Grs}, and X_{Pyr} and the values used are given in Table 2) and plagioclase (X_{Ab}) were calculated to aid with interpretation of the $P-T$ path. The proportion of Fe_2O_3 to FeO has been estimated by considering the abundance of Fe^{3+} bearing minerals and modal constraints in the context of recalculated EDS analyses (using the methods of Droop (1987) and Tindle and Webb (1994)). A $T-MFe_2O_3$ diagram was then calculated to determine if these estimates were appropriate. In the modeling of sample D04, the amount of Fe_2O_3 was decreased to remove magnetite from the retrograde assemblage. The percentage of total iron set as Fe^{3+} for samples MT3, V-1, D04, FQ15 (XRF) and FQ15 (calc) was 5%, 5%, 20.5%, 10% and 36% respectively. The $T-MFe_2O_3$ sections are included in the supplementary information (Supplementary Appendix 3).

The following mixing models and notations were applied: garnet, White et al. (2005); plagioclase, Holland and Powell (2003); biotite, White et al. (2005); white mica, Coggon and Holland (2002); ilmenite, White et al. (2005); chlorite, a combination of Mahar et al. (1997) and Holland and Powell (1998); epidote, Holland and Powell (1998); talc, Holland and Powell (1998); clinoamphibole/orthoamphibole, Diener et al. (2007); clinopyroxene, Green et al. (2007); magnetite-spinel, White et al. (2002); silicate melt, White et al. (2007); orthopyroxene, White et al. (2002). Rutile and quartz are also included as pure phases.

Zircon and titanite grains were separated for samples MT3, V-1, D04 and C03. Samples MT3 and V-1 contained zircon and titanite, whereas C03 contained only zircon, and D04 contained only titanite. Grains were mounted in epoxy and imaged using cathodoluminescence (CL) and back-scattered electron (BSE) imaging on a Jeol JSM-6510 scanning electron microscope with attached Centaurus CL detector. Titanite was also analyzed in situ from a thin section of sample D04. Zircon and titanite grains were analyzed with a laser ablation-inductively coupled plasma-mass spectrometry (LA-ICP-MS) system consisting of a Cetac 213 laser (with a tear drop shaped low volume sample cell) and Thermofinnigan Element 2 ICP-MS, hosted at the Universidade Federal de Ouro Preto. The data were acquired with single spot analyses employing 20 and 30 μm spot sizes for zircon and titanite respectively. Data acquisition was comprised of 20 s for background and 20 s of signal collection with 10 s wash out. The laser was operated at a repetition rate of 10 Hz and a measured energy output of 10%, corresponding to calculated laser energy of ∼0.02 mJ/pulse. Each individual spot analysis acquired counts on masses 202, 204, 206, 207, 208, 232, 235 and 238 during 40 runs, using electrostatic scanning (E-scan). The analytical run (∼1 s) integrates data of 20 individual intensity determinations (or "passes") of each isotope. Each pass consists of four individual intensity measurements across the flat top peaks of each mass, with the magnetic field resting at mass ^{202}Hg. The time-resolved raw data were exported from the ICP-MS in ASCII format and processed off-line with an Excel® spreadsheet (Gerdes and Zeh, 2006) and the Isoplot/Ex 3.00 software (Ludwig, 2003) was

Table 1
Bulk composition calculations.

Sample D04						
Mode	0.05	0.27	0.02	0.4	0.12	0.14	Total
Mineral	ilmenite	plagioclase	garnet	hornblende	cummingtonite	quartz	
SiO_2	0.15	56.55	37.65	44.68	51.79	100.00	54.11
TiO_2	51.19	0.00	0.01	1.06	0.07		2.99
Al_2O_3	0.09	26.98	21.58	10.85	1.35		12.22
Cr_2O_3	0.00	0.00	0.00	0.00	0.00		0.00
Fe_2O_3	0.00	0.00	0.00	10.74	0.08		4.31
FeO	44.98	0.14	30.28	10.00	28.19		10.27
MnO	0.57	0.00	1.18	0.06	0.36		0.12
MgO	0.00	0.00	3.23	9.09	13.35		5.30
ZnO	0.00	0.00	0.00	0.00	0.00		0.00
CaO	0.06	8.69	6.24	10.26	1.19		6.72
Na_2O	0.00	6.47	0.00	1.04	0.00		2.16
K_2O	0.00	0.07	0.00	0.03	0.00		0.03
H_2O	0.00	0.00	0.00	2.04	1.97		1.05
Total	97.04	98.89	100.17	99.85	98.36		99.30
Sample FQ15 - Fine-grained texture						
Mode	0.158	0.184	0.256	0.024	0.268	0.11	Total
Mineral	epidote	plagioclase	CPX	biotite	actinolite	quartz	
SiO_2	39.06	62.84	53.15	39.88	53.55	100.00	57.65
TiO_2	0.04	0.00	0.01	0.64	0.17		0.07
Al_2O_3	23.53	22.55	1.38	15.25	3.59		9.55
Cr_2O_3	0.14	0.00	0.01	0.00	0.02		0.03
Fe_2O_3	12.96	0.00	1.35	0.00	0.98		2.66
FeO	0.36	0.00	6.57	9.70	8.22		4.17
MnO	0.09	0.00	0.41	0.14	0.38		0.23
MgO	0.03	0.00	13.02	16.90	17.12		8.33
ZnO	0.00	0.00	0.00	0.00	0.00		0.00
CaO	23.64	4.24	23.37	0.00	12.82		13.94
Na_2O	0.11	9.23	0.71	0.32	0.37		2.00
K_2O	0.01	0.13	0.02	9.51	0.22		0.32
H_2O	0.00	0.00	0.00	5.00	2.11		0.69
Total	100.00	98.99	100.00	97.34	99.53		99.63

used for final age calculations and the plotting of results. The spreadsheet corrects for the respective background and subsequently the ^{206}Pb, ^{207}Pb and ^{208}Pb signals for common Pb using the background and interference corrected ^{204}Pb signal and a model Pb composition (Stacey and Kramers, 1975). Primary reference zircon M127 (TIMS normalization data $^{207}Pb/^{206}Pb = 526.8 \pm 0.2$ Ma, $^{206}Pb/^{238}U = 524.4 \pm 0.1$ Ma and $^{207}Pb/^{235}U = 524.8 \pm 0.1$ Ma; Mattinson, 2010) and titanite BLR-1 (TIMS normalization data $^{207}Pb/^{206}Pb = 1049.9 \pm 1.3$ Ma, $^{206}Pb/^{238}U = 1047.1 \pm 0.4$ Ma and $^{207}Pb/^{235}U = 1048.0 \pm 0.7$ Ma; Aleinikoff et al., 2007; Mazdab, 2009) were used for external corrections of inter-element fractionation and instrumental mass discrimination. The primary standards were analyzed under exactly the same conditions as the samples. A drift correction was applied by interpolation over a sequence of 12−20 standards (for 30−50 unknowns). Accuracy was checked using secondary standards GJ-1 (ca. 602 Ma; Jackson et al., 2004) and Plešovice (ca. 337 Ma; Sláma et al., 2008) for zircon, and

the Khan titanite standard (ca. 520 Ma; Kinny et al., 1994; Heaman, 2009). Over the duration of the study, the average normalized ages for M127 were $^{207}Pb/^{206}Pb = 525.7 \pm 5.4$ Ma, $^{206}Pb/^{238}U = 525.4 \pm 0.8$ Ma and $^{207}Pb/^{235}U = 525.4 \pm 0.9$ Ma ($n = 85$) and the weighted average $^{206}Pb/^{238}U$ age for GJ-1 and Plešovice were 604 ± 2 Ma and 338 ± 2 Ma respectively. The titanite BLR-1 standard gave normalization ages of $^{207}Pb/^{206}Pb = 1050 \pm 3$ Ma, $^{206}Pb/^{238}U = 1049 \pm 3$ Ma and $^{207}Pb/^{235}U = 1049 \pm 3$ Ma ($n = 22$) and the weighted average $^{206}Pb/^{238}U$ age for Khan was 515 ± 2 Ma. All data is given in Supplementary Table 1.

7. Results

7.1. Sample petrography and mineral chemistry

7.1.1. Sample MT3 − garnet-gedrite schist

Sample MT3 contains garnet, gedrite, biotite, ilmenite, plagioclase, quartz and minor chlorite, apatite, tourmaline and rutile (Fig. 4A and B). Garnet grains are large (up to 1 cm in size) and appear to be zoned at least in their inclusion abundance. Garnet contains inclusions of quartz, plagioclase, ilmenite, biotite, rutile and chlorite. Chlorite occurs on garnet rims and cracks within garnet grains (Fig. 4B). More abundant, fine inclusions of ilmenite occur in the garnet cores and coarser inclusions of quartz occur in the rim or the boundary between cores and rims. Rutile is found almost exclusively as inclusions within garnet and gedrite while ilmenite occurs as inclusions in garnet and gedrite cores, as well as in the matrix (Fig. 4A and B). Gedrite grains are up to 5 mm in size and contain inclusions of quartz, ilmenite and rutile. On cracks and

Table 2
Garnet compositions used for isopleths.

MT3							
X_{grs}	0.07-0.11	X_{sps}	0.01-0.04	X_{alm}	0.63-0.77	X_{pyr}	0.11-0.25
X_{Ab}[a]	0.57-0.58	X_{Ab} core	0.62-0.64	X_{Ab} rim	0.71-0.77		
V-1							
X_{grs}	0.14-0.16	X_{sps}	0.03-0.05	X_{alm}	0.64-0.73	X_{pyr}	0.09-0.17
X_{Ab}[a]	0.53-0.66	X_{Ab} core	0.3-0.41				
D04							
X_{grs}	0.16-0.2	X_{sps}	0.02-0.04	X_{alm}	0.65-0.71	X_{pyr}	0.1-0.14
X_{Ab} core	0.62	X_{Ab} late[b]	0.5-0.53				

[a] Inclusion in garnet.
[b] Rim values or from grains on cracks in garnet.

grain edges, gedrite is replaced by anthophyllite and/or chlorite (Fig. 4A). Gedrite, biotite and ilmenite define the foliation of the sample. However, in some areas of the sample, fine-grained biotite is randomly oriented and perhaps grew at the expense of garnet or gedrite (Fig. 4B). Plagioclase is up to 2 mm in size and is sericitized on grain rims and along cracks.

Garnet grains in sample MT3 have a complex zonation (Fig. 5A). Based on changes in slope in the X_{Grs}, X_{Alm} and X_{Pyr} profiles, the garnet grains have been split into two zones (Fig. 5A). The grain core is zone 1 and the grain rim is zone 2. In zone 1 X_{Sps} (=Mn/(Fe + Mg + Mn + Ca)) is high in the core (0.04) and drops toward the edge of the zone (to 0.02). In zone 2, at about 1 mm from the rim, X_{Sps} drops to 0.01 and then increases again up to 0.02 on the edge of the grain. In zone 1, X_{Grs} (=Ca/(Fe + Mg + Mn + Ca)) is high in the core (0.11) then drops toward the edge of the zone (to 0.07). In zone 2, X_{Grs} is high again (0.1) before dropping to 0.08 on the very edge of the grain. In zone 1 X_{Pyr} (=Mg/(Fe + Mg + Mn + Ca)) gradually increases from the core (0.11–0.13). In zone 2, X_{Pyr} is ca. 0.17 until about 500 μm from the edge of the grain, where it increases abruptly to 0.25. In zone 1, X_{Alm} (=Fe/(Fe + Mg + Mn + Ca)) also gradually increases from 0.73 in the core up until 0.77. In zone 2, X_{Alm} is ca. 0.73 until 500 μm from the grain rim when it drops abruptly to 0.64. Of the two amphiboles in sample MT3, gedrite has an X_{Mg} (=Mg/(Fe + Mg)) of 0.51–0.59, whereas anthophyllite has an X_{Mg} of 0.55–0.6. Biotite in sample MT3 has X_{Mg} of 0.67–0.69 and TiO$_2$ contents of 1.42–1.86 wt.%. Matrix plagioclase grains in sample MT3 have X_{Ab} (=Na/(Na + Ca + K)) values of 0.61–0.73. Cores generally have no zonation (0.62–0.64) while higher values are found on cracks and grain rims. Plagioclase grains which occur as inclusions within garnet have X_{Ab} values of 0.57–0.58. Plagioclase grains intergrown with chlorite on garnet rims and on cracks within garnet have X_{Ab} of 0.71–0.77. Ilmenite in sample MT3 contains 0–0.35 wt.% MnO, 0–0.73 wt.% MgO and recalculated analyses contain no detectable Fe$_2$O$_3$. In sample MT3, chlorite has X_{Mg} of 0.62–0.71.

7.1.2. Sample V-1 − garnet-bearing amphibolite

This sample contains garnet, hornblende, plagioclase, quartz, cummingtonite and ilmenite with minor biotite, muscovite, apatite and chlorite (Fig. 4C and D).

Garnet in this sample is sparse but large (up to 1 cm) and poikiloblastic with inclusions of quartz, ilmenite, hornblende, biotite and plagioclase (Fig. 4C). Garnet contains S-shaped inclusion trails which are not continuous with the matrix foliation. Biotite is rare and occurs only on cracks within and on the edges of garnet (Fig. 4C). Garnet has irregular grain edges and hornblende grains next to garnet are coarser (up to 1 mm in size; Fig. 4C). Hornblende has straight contacts with garnet while cummingtonite is not observed in contact with garnet.

The matrix of the sample is reasonably equigranular with hornblende and quartz being around 400 μm while plagioclase and cummingtonite are around 200 μm and ilmenite is up to 100 μm. Plagioclase, ilmenite and hornblende grains are elongate and define the matrix foliation. Cummingtonite grains are associated with hornblende and are euhedral and equigranular (Fig. 4D). In some cases, hornblende is observed surrounding cummingtonite while in other cases cummingtonite seems to partially replace hornblende. In some regions of the matrix, both amphiboles are surrounded by fine-grained reaction rims, which contain plagioclase, epidote and white mica. In one instance, a grain of titanite was observed next to one of these textures on a crack in a hornblende grain.

Minor chlorite occurs with biotite on cracks within garnet grains. Muscovite occurs in some matrix plagioclase grains.

Garnet in sample V-1 is unzoned with X_{Alm} values of 0.64–0.73 (Fig. 5B). The rim values are slightly higher (0.66–0.70) than the

grain cores (0.64–0.66). The wide range of values is possibly related to the presence of cracks and inclusions. X_{Sps} values vary from 0.03 (on grain rim) to 0.045, X_{Pyr} varies from 0.09 to 0.17 with a range of values throughout the grain, although on the grain rims the values are generally higher. X_{Grs} values vary from 0.14 to 0.16. Most amphibole grains in sample V-1 are Fe-Mg-Ca amphiboles that are classified as ferri-magnesio-hornblende to ferri-tchermakitic hornblende. These grains have X_{Mg} values of 0.56–0.78 and complex zoning with low core values (0.58), which rise to 0.75, then drop to 0.6 before rising again on grain rims (0.65–0.72). These hornblende grains have TiO$_2$ content of 0.36–1.12 wt.% and a recalculated Fe$_2$O$_3$ content of 4.12–14.31 wt.%. The second amphibole is an Fe-Mg rich but Al-poor amphibole which is classified as cummingtonite with X_{Mg} values of 0.51–0.53. Biotite in sample V-1 has X_{Mg} of 0.54–0.58 and TiO$_2$ content of 1.40–1.97 wt.%. Plagioclase has X_{Ab} of 0.17–0.66. Matrix plagioclase grains have lower X_{Ab} (0.17–0.41) with higher values usually occurring on grain rims (0.30–0.41) or near cracks in grains. Plagioclase that occurs sealed within quartz grains, which are in turn included in garnet have X_{Ab} values similar to matrix grains (0.22–0.33). Grains on a crack in garnet which are intergrown with biotite have the highest X_{Ab} values (0.46–0.66). Ilmenite in sample V-1 contains 0.39–0.46 wt.% MnO and no detectable Fe$_2$O$_3$. In sample V-1, chlorite has an X_{Mg} of 0.62–0.66.

7.1.3. Sample D04 − garnet-bearing amphibolite

This sample contains garnet, hornblende, cummingtonite, plagioclase, quartz and ilmenite with minor apatite (Fig. 4E and F).

Hornblende grains are sub to euhedral, up to 500 μm in size and contain inclusions of ilmenite, apatite and quartz (Fig. 4E). Cummingtonite commonly occurs on the grain rims of hornblende or in contact with it (commonly where hornblende is bordered by quartz). It is subhedral and up to 100 μm in size (Fig. 4F). Garnet grains are small (up to 2 mm and rounded or blobby) and contain inclusions of quartz, hornblende, plagioclase and ilmenite (Fig. 4E). Hornblende and cummingtonite are rarely observed in contact with garnet. Often they appear to be in contact but are in fact separated by a thin layer of plagioclase (Fig. 4F). Garnet is commonly surrounded by a zone of plagioclase, quartz and ilmenite, which commonly separates garnet from hornblende. Plagioclase grains are up to 400 μm in size and contain inclusions of quartz, ilmenite and hornblende. Finer-grained plagioclase occurs on the rims of garnet.

Garnet in sample D04 does not have a distinct zonation (Fig. 5C and D). X_{Sps} is slightly higher in grain cores and on the grain rim and varies from 0.035–0.02. X_{Pyr} varies from 0.1 to 0.14, with the lowest values being recorded in grain cores (0.1–0.14) and also the outermost rim (to 0.12). X_{Grs} varies from 0.16 to 0.2. Low values are found on grain rims (0.17), however, in some cases cores also have low values with a high between the core and the rim, while in other grains the high values occur at the grain core. X_{Alm} varies from 0.65 to 0.71. Higher values occur at grain rims and also in the core of some grains. Most amphibole grains in sample D04 are Fe-Mg-Ca amphiboles and classified as ferri-magnesio-hornblende. These grains have X_{Mg} of 0.51–0.75 with lower values generally occurring on grain rims. This type of amphibole also contains TiO$_2$ of 0.81–1.29 wt.% and Fe$_2$O$_3$ (recalculated) of 6.67–17.04 wt.%. The second amphibole is an Fe-Mg rich but Al-poor amphibole that is classified as cummingtonite. This has X_{Mg} of 0.45–0.46 with 0–0.3 wt.% TiO$_2$ and 0–0.61 wt.% Fe$_2$O$_3$. Biotite in sample FQ15 has X_{Mg} of 0.75–0.76 and TiO$_2$ contents of 0.54–0.73 wt.%. Plagioclase has X_{Ab} of 0.51–0.62. The highest values occur in grain cores (up to 0.62) and lower values on the rims (ca. 0.51–0.53). Plagioclase grains which surround garnet have higher X_{Ab} (ca.

0.69). Ilmenite in sample D04 contains 0.54−0.62 wt.% MnO and 0−0.58 wt.% Fe_2O_3. Epidote has pistacite contents (X_{Ps} = Fe^{3+}/(Fe^{3+}+Al)) of 0.15−0.21.

7.1.4. Sample FQ15 − migmatized amphibolite dike

This sample contains hornblende, clinopyroxene, actinolite, plagioclase, quartz and epidote with minor biotite, titanite and ilmenite (Fig. 4G).

Clinopyroxene grains are subhedral and up to 2 cm in size. Clinopyroxene contains inclusions of hornblende, quartz and ilmenite. Where hornblende inclusions occur on cracks in the grain, the inclusions are rimmed by actinolite with hornblende cores (Fig. 4H). Hornblende is subhedral and up to 1 cm in size. Hornblende defines the foliation of the sample and contains inclusions of quartz and ilmenite. Titanite and epidote commonly occur on cracks within hornblende or on the boundaries of hornblende grains. In these locations, hornblende is often rimmed with actinolite (Fig. 4G and H). Where clinopyroxene and hornblende have grain boundaries with plagioclase, symplectitic intergrowths (10−100 μm in size) of quartz and epidote occur. These intergrowths are frequently associated with actinolite, which appears to pseudomorph clinopyroxene or amphibole (Fig. 4G and H). Plagioclase is anhedral and up to 1 cm in size. Biotite is euhedral and forms narrow blades, crosscutting the foliation. It can also occur as fine grains between amphibole grains (Fig. 4H).

Most amphibole in sample FQ15 is Fe-Mg-Ca amphibole and typically classified as magnesio-hornblende. These grains have X_{Mg} of 0.66−0.71 with no apparent compositional zonation. This type of amphibole also contains TiO_2 of 0.50−0.88 wt.% and Fe_2O_3 (recalculated) of 0−4.04 wt.%. The second amphibole is an Fe-Mg rich but Al-poor amphibole which is classified as actinolite. This has X_{Mg} of 0.79−0.86 with up to 1.89 wt.% Fe_2O_3. Plagioclase has X_{Ab} of 0.76−0.96. The highest values occur on grain rims where fine-grained epidote occurs (0.80−0.96). The cores are generally unzoned (ca. 0.76−0.78). Clinopyroxene has high CaO content (22.0−24.5 wt.%), resulting in a wollastonite component close to 50 wt.% and Mg# varying from 0.75 to 0.83. Chemical traverses reveal core-to-rim homogeneous composition. Epidote has variable pistacite contents (X_{Ps} = Fe^{3+}/(Fe^{3+}+Al)) with values ranging from 0.14 to 0.38. High values come exclusively from grain cores.

7.2. Metamorphic petrology

7.2.1. Sample MT3-garnet-gedrite schist

This sample contains an interpreted peak assemblage of garnet + gedrite + plagioclase + quartz + rutile + biotite. This occurs on the phase diagram at 5−10 kbar and 625−700 °C (field outlined in bold, Fig. 6A). This field is bound by cordierite on the low pressure side, kyanite at high pressure and melt at high temperature. Based on the mineral assemblage evolution, with early garnet and gedrite containing inclusions of chlorite and ilmenite followed by rutile and the absence of matrix chlorite (except as a retrograde feature), an up-pressure and temperature P−T path can be defined. Since we have no inclusion relationships between garnet and gedrite, it is impossible to know which of these grew first so there is uncertainty in the slope of the path (Fig. 6A). Garnet and plagioclase compositional isopleths, and garnet isomode lines were calculated for the diagram. The maximum temperatures indicated by the location of the peak assemblage field of 600−700 °C imply that garnet compositions may have been partially re-equilibrated. Since this P−T pseudosection was calculated using the whole-rock composition, only the garnet core composition (zone 1) can be used to determine the P−T evolution (Palin et al., 2016). The position where the garnet core composition isopleths meet occurs near the garnet-in line

(Fig. 6B). The change in X_{Grs} composition from core to rim of the garnet (from 0.11 to 0.07), as well as the decrease in X_{Sps} and increase in X_{Pyr} also indicate an up-pressure and temperature path (blue arrow, Fig. 6B). When the X_{Ab} and garnet mode information is added, peak conditions of 8−9 kbar at 650−700 °C are indicated by the composition of plagioclase cores (the rims are affected by retrogression and indicate much higher values; Fig. 6C). The X_{Ab} values of plagioclase in garnet are also consistent with the up-pressure and temperature path (Fig. 6C). The bend in the path is defined by the flat X_{Ab} compositional profiles in plagioclase (a further increase in pressure would result in a change in composition, which is not observed) and the absence of melt in the sample. The retrograde segment of the path is defined by late chlorite, the presence of matrix ilmenite and absence of rutile, and the high X_{Ab} values found on plagioclase rims and along grains cracks. Since these may have occurred in a different effective bulk composition, the retrograde path is poorly defined (Fig. 6C). The interpreted P−T path is a clock-wise path resulting in peak conditions of 650−700 °C and 8−9 kbar with the retrograde path passing through the rutile absent field and then into the chlorite bearing field (Fig. 6).

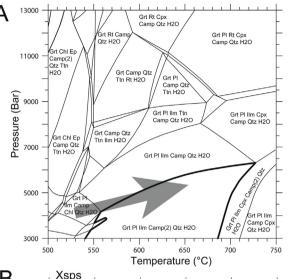#### 7.2.2. Sample V-1 − garnet-bearing amphibolite

The interpreted peak assemblage for this sample is garnet + hornblende + cummingtonite + quartz + plagioclase + ilmenite, which occurs on the calculated phase diagram for this sample at 2−6 kbar and 550−720 °C (Fig. 7A). Camp (2) indicates that this field contains two clinoamphiboles, whereas the field above this contains only the aluminum-rich clinoamphibole (hornblende in this case; Fig. 7A). Garnet isopleths were plotted for this sample; however, the calculated X_{Alm} values are somewhat lower than those found in the sample (0.42−0.65 vs. 0.64−0.73). In contrast, the X_{Grs} isopleths were higher on the diagram than the compositions found in the sample (0.20−0.46 vs. 0.14−0.16). However, the highest X_{Alm} values present on the diagram, along with the X_{Pyr} and X_{Sps} composition overlap within the peak field (Fig. 7B) indicating maximum conditions of 650−700 °C at 6 kbar. The P−T path is defined by: the addition of cummingtonite in the mineral assemblage (Fig. 7A); the position of the garnet composition (Fig. 7B); the position of the plagioclase composition (Fig. 7C); and the increase in garnet mode (Fig. 7C). The retrograde portion of the path is defined by the presence of late chlorite and the higher X_{Ab} compositions of plagioclase, which occur on cracks within garnet grains. The fine-grained aggregate of epidote + white mica ± titanite that replace plagioclase occurs in a lower temperature field. This lower temperature assemblage may be part of the same P−T evolution; however, the whole-rock bulk composition of the sample is not appropriate for modeling these, or producing the observed rim composition of plagioclase, which is not present on the diagram.
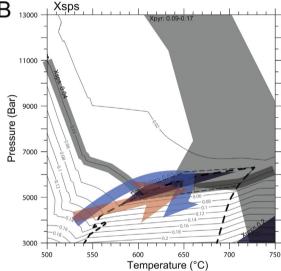
Thus, although poorly constrained, this sample seems to record a near-isobaric P−T evolution culminating in peak conditions of 6 kbar and 650 °C (Fig. 7C).

7.2.3. Sample D04 − garnet-bearing amphibolite

The interpreted peak assemblage of this sample is garnet + hornblende + plagioclase + quartz + ilmenite which occurs on the calculated phase diagram at 6−10 kbar and 620−740 °C (Fig. 8A). The field below the peak field contains two clinoamphiboles, as indicated by Camp (2), whereas the interpreted peak field contains only the aluminum-rich clinoamphibole (hornblende in this case; Fig. 8A). As with previous samples, garnet isopleths were calculated and again X_{Alm} does not match between the P−T pseudosection and the sample. However, the highest X_{Alm} values present on the diagram and the X_{Pyr}, X_{Grs} and X_{Sps} compositions

Sample V-1: Si(50.16)Al(16.19)Ti(0.55)Fe(11.43)F3(0.11)
Mg(8.72)Mn(0.18)Ca(9.92)Na(2.73)H(40)
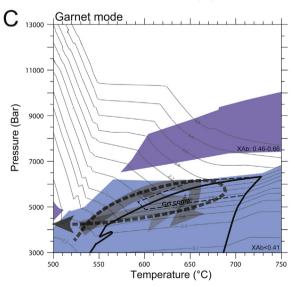
measured in the sample, overlap in the low-pressure, high-temperature part of the peak field (Fig. 8B). The $P-T$ path for this sample is defined by: 1) the change in mineral assemblage, this being the addition of garnet to the peak assemblage followed by the addition of cummingtonite that appears to be later than garnet (Fig. 8A); 2) the garnet composition, which overlaps the peak field at conditions of ca. 700 °C and 7 kbar (Fig. 8B); and 3) the change in plagioclase composition between core and rim, and the presence of plagioclase coronas on garnet rims (separating garnet from amphibole) that indicates decompression (Stowell and Stein, 2005, Fig. 8C).

Taken together, it appears that the sample experienced a clockwise $P-T$ path with peak conditions of 7 kbar and 700 °C (Fig. 8C).

7.2.4. Sample FQ15 − migmatized amphibolite dike

This sample appears to contain a coarse-grained assemblage of hornblende + clinopyroxene + plagioclase + quartz + ilmenite + melt, based on the presence of large clinopyroxene grains within the felsic leucosomes present in the outcrop (Fig. 3D). Since the sample has melted, it is possible that some melt loss has occurred. Thus, in order to model the melting event, two diagrams were created using the XRF composition of the sample. The first (Fig. 9A) has H_2O set such that the solidus is just hydrated. This diagram should indicate the $P-T$ evolution of the sample prior to melting, and in the case that melt is retained. A second diagram with a dry solidus is presented in Fig. 9B. This presents a simplified scenario should melt have been lost from the system during the $P-T$ evolution. In both diagrams the interpreted peak assemblage field occurs just above the solidus, at 5−8 kbar and 700 °C, and 3.5−7 kbar and 700−750 °C in Fig. 9A and B, respectively. It is constrained by garnet-in at higher pressures, the solidus at low temperature, and two-amphibole or orthopyroxene-bearing fields at higher temperatures (Fig. 9A and B). The $P-T$ path presented in Fig. 9A is defined by the increase in mode of clinopyroxene.

On the rims of clinopyroxene and amphibole grains, where plagioclase is present, a fine-grained assemblage of epidote + actinolite + quartz + biotite + titanite + albitic plagioclase occurs (Fig. 4H). A third diagram was calculated using the composition of one of these domains in order to model the $P-T$ conditions of formation. It is possible that these reactions were limited by the availability of H_2O, i.e. they only occurred where H_2O was present in the sample. For this reason, H_2O was set such that it is present in most of the subsolidus fields (Fig. 9C). The interpreted

the internally consistent dataset of Holland and Powell (1998). The interpreted peak field has a bold outline while a grey arrow indicates the prograde $P-T$ path based on the change in mineral assemblage of the sample. Mineral abbreviations as in Kretz (1983) except clinoamphibole which is abbreviated as Camp. Camp (2) indicates that two clinoamphibole with different compositions are stable. (B) Compositional isopleths for X_{Sps} are given in grey. The grey fields are the composition of the garnet from sample V1. The bold black dashed field is the interpreted peak assemblage of the sample. The red arrow indicates the $P-T$ evolution for the sample based on the change in mineral assemblage, whereas the blue arrow is the $P-T$ evolution for the sample based on the location of the garnet composition as well as the change in mineral assemblage. (C) Garnet mode (in mol) for sample V1 are given in grey. The blue fields indicate the composition of plagioclase from this sample. The lighter blue field shows the X_{Ab} composition of matrix plagioclase. The darker blue field shows the X_{Ab} composition of plagioclase found with biotite on cracks in garnet grains. The garnet core composition is shown by the dashed field. The field outlined in bold indicates the position of the interpreted peak field. The dashed black arrow indicates the interpreted $P-T$ path for this sample. This is defined by the mineral assemblage evolution with the growth of garnet and hornblende stability both before and after cummingtonite as well as the composition of plagioclase and garnet. The $P-T$ paths based on the mineral assemblage evolution and the change in garnet composition are also given in grey.
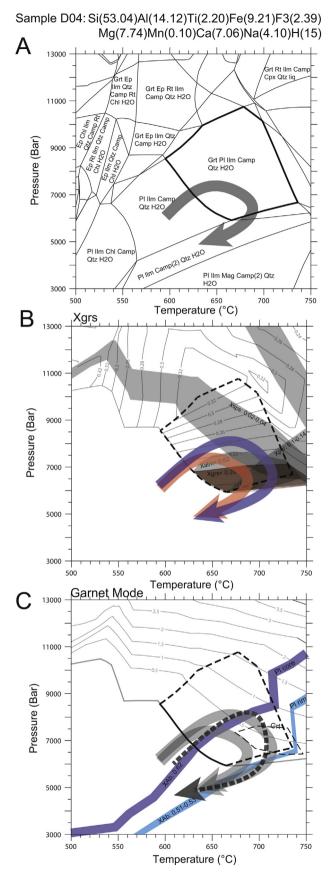
Figure 7. (A) Calculated $P-T$ pseudosection for sample V-1 based on the whole rock composition that is given at the top of the diagram in moles. The diagram was created using the Theriak-Domino software package (De Capitani and Petrakakis, 2010) with

Figure 8. (A) Calculated $P-T$ pseudosection for sample D04 based on a calculated composition, which is presented at the top of the diagram in moles. The diagram was created using the Theriak-Domino software package (De Capitani and Petrakakis, 2010)

peak assemblage field of plagioclase + hornblende + clinopyroxene + actinolite + quartz + titanite + epidote + biotite occurs in this diagram at 4−9 kbar and 550−600 °C. This is quite a large pressure range so compositional isopleths of plagioclase were plotted to constrain the $P-T$ position of the fine-grained assemblage. The field in blue on Fig. 9C indicates where plagioclase with $X_{Ab} > 0.8$ occurs and suggests peak $P-T$ conditions of 8−9 kbar and 550 °C for the fine-grained assemblage. Fig. 9D shows a compilation of the $P-T$ data from sample FQ15. The early coarse-grained assemblage has two fields (H_2O present and absent) and a poorly defined $P-T$ path based on the increase in clinopyroxene mode (H_2O present). The retrograde portion of the path corresponds to the stability of two amphiboles. However, it is possible that the two amphiboles are not stable together but rather one is related to each $P-T$ evolution (Fig. 9D).

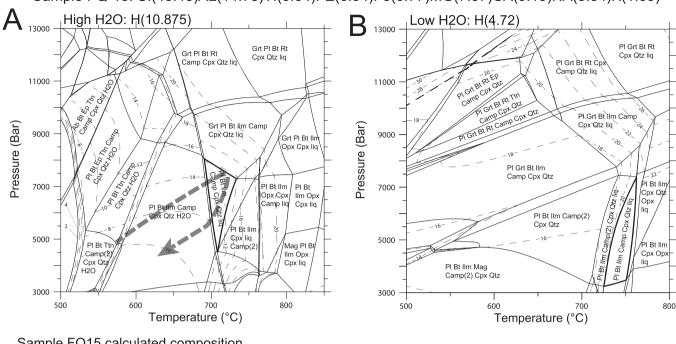### 7.3. U−Pb geochronology

7.3.1. Sample MT3 − garnet-bearing schist

This sample yielded a large amount of zircon and titanite grains. Zircons were relatively small (<150 μm), pink transparent grains. Some grains preserve long prismatic shapes, but many are broken in half and show round terminations. CL images reveal poorly developed zoning (Fig. 10A). The grains are marked by structureless patchy interiors with bright and dark domains. A limited number of grains show core-rim relationships, i.e. structureless/patchy cores surrounded by oscillatory rims (Fig. 10A). LA-ICP-MS spots on the irregular cores gave $^{206}Pb/^{207}Pb$ ages of ca. >2900 Ma (Fig. 10A). Twelve out of fourteen spots (Supplementary Table 1) on the cores define a discordia line with an upper intercept age of 2999 ± 13 Ma (MSWD = 4.5; Fig. 10B). Analyses on the structureless grains, with both dark and bright domains, gave points that are discordant to slightly concordant (Fig. 10A and B). The most concordant points align along a recent, Pb-loss discordialine that intercepts the concordia at 2775 ± 6 Ma (MSWD = 2.2; Fig. 10B).

The core age of 2999 ± 13 Ma is interpreted as a detrital population while the younger age of 2775 ± 6 Ma is interpreted as metamorphic, however it cannot be excluded that this is an additional detrital population. Alternatively, if the origin of this unit is volcaniclastic, this age may reflect extrusion, giving the age of deposition.

Titanites for this sample are light brown, transparent and irregular in shape. Under BSE imaging they show simple or blocky to compositional zoning, with no inherited cores or other complicating structures. U−Pb results were obtained from a total of eleven titanite analyses on different grains (Supplementary Table 1). All data plot in a coherent group, with the variation in precision directly reflecting the

with the internally consistent dataset of Holland and Powell (1998). The interpreted peak field has a bold outline while a grey arrow indicates the prograde $P-T$ path based on the change in mineral assemblage of the sample. Mineral abbreviations as in Kretz (1983) except clinoamphibole which is abbreviated as Camp. Camp (2) indicates that two clinoamphibole with different compositions are stable. (B) Compositional isopleths for X_{Grs} are given in grey. The grey fields are the composition of the garnet from sample D04. The bold black dashed field is the interpreted peak assemblage of the sample. The red arrow indicates the $P-T$ evolution for the sample based on the change in mineral assemblage, whereas the blue arrow is the $P-T$ evolution for the sample based on the location of the garnet composition as well as the change in mineral assemblage. (C) Garnet mode (in mol) for sample D04 are given in grey. The blue fields indicate the composition of plagioclase from this sample. The darker blue field shows the X_{Ab} composition of plagioclase cores, whereas the lighter blue field shows the X_{Ab} composition of plagioclase rims. The garnet core composition is shown by the thin dashed field. The field outlined in bold dashes indicates the position of the interpreted peak field. The dashed black arrow indicates the interpreted $P-T$ path for this sample defined by the mineral assemblage evolution with the growth of garnet, late cummingtonite, as well as the composition of plagioclase and garnet. The $P-T$ paths based on the mineral assemblage evolution and the change in garnet composition are also given in grey.

Sample FQ-15: SI(48.45)AL(14.78)TI(0.64)FE(6.94)F3(0.77)MG(7.57)CA(9.19)NA(5.84)K(1.09)
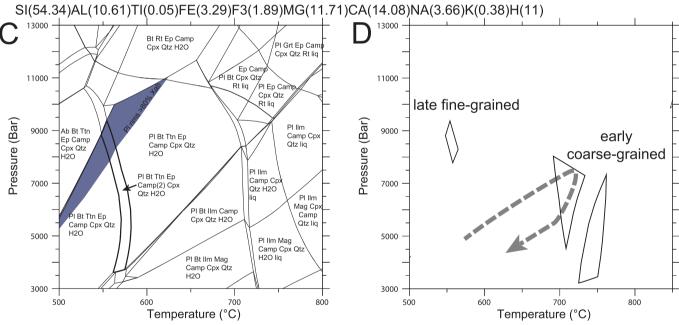

Sample FQ15 calculated composition
SI(54.34)AL(10.61)TI(0.05)FE(3.29)F3(1.89)MG(11.71)CA(14.08)NA(3.66)K(0.38)H(11)

Figure 9. (A) Calculated $P-T$ pseudosection for sample FQ15 based on the whole-rock composition with the H_2O content set such that the solidus is just saturated with H_2O. The H_2O value used is given at the top of the diagram and the composition used for Fig. 9A and B is presented at the top of the diagram in moles. The diagram was created using the Theriak-Domino software package (De Capitani and Petrakakis, 2010) with the internally consistent dataset of Holland and Powell (1998). The interpreted peak field has a bold outline. The thin, dashed line indicates clinopyroxene mode in vol.%, whereas the thick grey dashed arrow indicates the prograde $P-T$ path based on the increase in clinopyroxene mode. (B) A second $P-T$ pseudosection for sample FQ15, using the whole-rock composition but a lower H_2O value (assemblages below the solidus and the solidus are dry). The H_2O value used is given at the top of the diagram and otherwise the composition used is identical to that of Fig. 9A. The interpreted peak field has a bold outline. The thin, dashed line indicates clinopyroxene mode in vol.%. (C) Calculated $P-T$ pseudosection for sample FQ15 based on a calculated composition, which is presented at the top of the diagram in moles. The diagram was created using the Theriak-Domino software package (De Capitani and Petrakakis, 2010) with the internally consistent dataset of Holland and Powell (1998). The interpreted peak field has a bold outline. The blue field indicates the location of plagioclase compositions that correspond to those found within the fine-grained textures. Mineral abbreviations as in Kretz (1983) except clinoamphibole which is abbreviated as Camp. Camp (2) indicates that two clinoamphibole with different compositions are stable. (D) Compilation of the P-T data from sample FQ15.

wide range in U contents of between 19 and 50 ppm (Fig. 10C; Supplementary Table 1). As a group, the data (11 points) are concordant to slightly discordant but give a weighted mean $^{206}Pb/^{238}U$ age of 2037 ± 17 Ma (MSWD = 1.7, $n = 11$; Fig. 10C), whereas nine concordant grains give a concordia age of 2042 ± 11 Ma.

7.3.2. Sample V-1 — garnet-bearing amphibolite

Sample V-1 of the fine-grained amphibolite contained zircon and titanite. Zircons display short prismatic to round shapes. All grains range in color from dark brown to slight translucent brown and are marked by bright luminescence under the CL detector
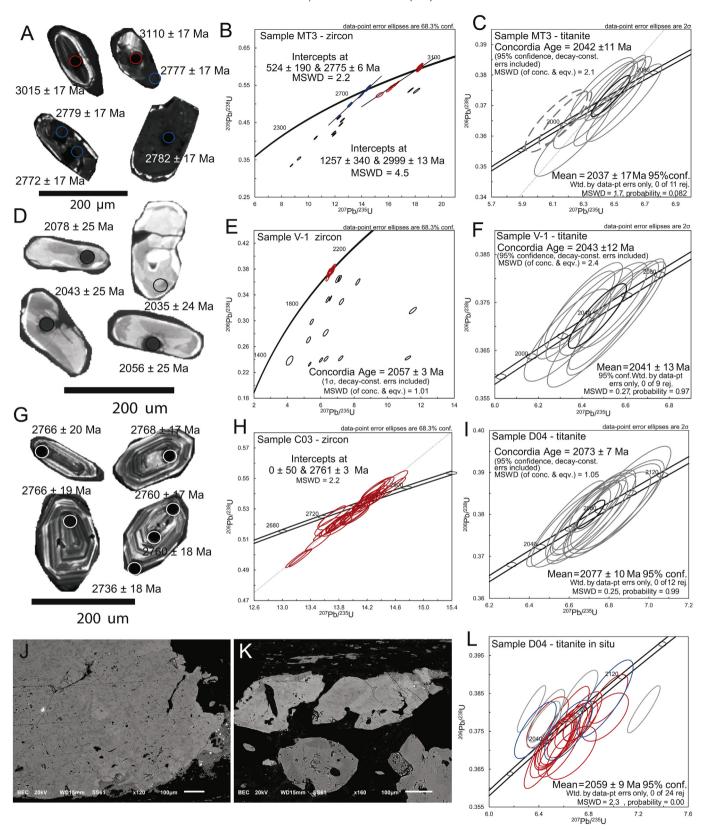
Figure 10. (A) CL images of zircon grains from sample MT3. Blue spots indicate rim or structureless analyses while red spots indicate grain cores. $^{207}Pb/^{206}Pb$ ages are given for each of the spots. (B) Concordia plot of zircon from sample MT3. (C) Concordia plot of titanite from sample MT3, the concordia age does not include the two dashed analyses. The mean of the $^{206}Pb/^{238}U$ age included all analyses. (D) CL images of zircon grains from sample V1. $^{207}Pb/^{206}Pb$ ages are given for each of the spots. (E) Concordia plot of zircon from sample V-1, the concordia age is for the analyses given in red.(F) Concordia plot of titanite from sample V-1 with the concordia age and mean $^{206}Pb/^{238}U$ age of all analyses. (G) CL images of zircon from sample C03. $^{207}Pb/^{206}Pb$ ages are given for each of the spots. (H) Concordia plot of zircon from sample C03. (I) Concordia plot of titanite from sample D04 with the concordia age and mean $^{206}Pb/^{238}U$ age of all analyses. (J) BSE image of a portion of coarse-grained titanite in sample D04. (K) BSE image showing zonation in finer-grained titanite in sample D04. (L) Concordia plot of in situ titanite analyses from sample D04 with the weighted mean $^{206}Pb/^{238}U$ age.

(Fig. 10D). No core-rim relationship was clearly observed. A number of round zoned grains gave highly discordant points with ^{206}Pb/^{207}Pb apparent ages ranging from 2300 Ma to 2600 Ma. Other small (>100 μm) transparent grains were clearly structureless or patchy zoned under CL imaging. Most grains gave concordant points that define a concordia age of 2057 ± 6 Ma (n = 17; Fig. 10E). The age of 2057 ± 6 Ma is interpreted as metamorphic. This is supported by consistent low Th/U ratios obtained from analyses that give this age (Supplementary Table 1).

As with sample MT3, titanites from this sample were light green to brown, transparent and irregular in shape. BSE images reveal patchy compositional zoning, with no inherited cores or other complicating structures. U−Pb results were obtained from a total of eleven titanite analyses on different grains (Supplementary Table 1). Nine titanites gave concordant points with a concordia age of 2043 ± 12 Ma (Fig. 10F).

7.3.3. Sample C03 − amphibolite dike

This amphibolite dike (Sample C03) crosscuts felsic schists in the southern part of the Bação complex. It contains pink, transparent zircons ranging in size from 100 to 300 μm (Fig. 10G). Most grains were prismatic to short prismatic with round edges. CL images show well defined oscillatory zoning. No cores were observed but thin metamorphic rims are visible on many grains, however, these were too thin to date (Fig. 10G). Analyses on the edges and center of several prismatic zoned grains gave concordant to subconcordant points with a similar range of apparent ages (Supplementary Table 1; Fig. 10G and H). The points align along a discordia line that intercepts the upper concordia at 2761 ± 3 Ma (MSWD = 2.2; Fig. 10H), when the lower intercept is anchored at zero. This is interpreted to be the crystallization age for this sample.

7.3.4. Sample D04 − garnet-bearing amphibolite

Sample D04 of the coarse-grained amphibolite from the central part of the Bação complex yielded a number of >200 μm yellow titanite grains, but no zircon. The titanite did not show visible zoning under BSE. However, the grains contain abundant inclusions of silicate phases and are commonly fractured. Several LA-ICP-MS analyses show low U and Th concentrations, ranging between 10−112 ppm and 1−12 ppm, respectively (Supplementary Table 1). The U−Pb analyses plot as a group with variable discordance of between 1% and 4%. U−Pb data from 12 spot analyses gave a concordia age of 2073 ± 7 Ma (Fig. 10I).

Data was also collected from titanite in a thin section from sample D04. Three grains were analyzed, one coarse grained titanite crystal (>2 cm in length, Fig. 10J), and two fine-grained titanite grains (200−300 μm) that were intergrown with the matrix minerals of the sample. BSE imaging indicated that the large grain has patchy zonation with darker domains on the grain edge. The finer matrix grains display some patchy internal zonation and rim domains (Fig. 10K). This zoning does not seem to relate to age with analyses from all grains giving the same age within uncertainty (Fig. 10L). The weighted mean ^{206}Pb/^{238}U age is 2059 ± 9 Ma (MSWD = 2.3, n = 24; Fig. 10L).

8. Discussion

8.1. Age and nature of metamorphism

Zircon and titanite geochronology of the samples in this study result in a range of ages.

In sample MT3, zircon grains have complex textures with dark and bright bands making it difficult to discern the zoning of grains. Older ages are recorded from the center of grains (Fig. 10A). In some cases, grains that have old cores, also have a dark rim, which gives a younger age. Many of the younger ages are obtained from dark, structureless rims although there are also complexly zoned grains that give young ages (Fig. 10A). Th/U ratios for zircon in sample MT3 are indistinguishable between the older (ca. 2999 Ma) and younger population (ca. 2775 Ma; Supplementary Table 1). However, it is possible for metamorphic zircon to have higher Th/U ratios or to inherit the Th/U ratio of the inherited magmatic population (e.g. Möller et al., 2003), so this does not preclude the younger group from being metamorphic. Given the upper amphibolite facies grade of the sample and the general occurrence of the younger ages on structureless rims, we interpret the younger population to be metamorphic. Although, it is worth noting that the Nova Lima Group contains volcaniclastic greywackes that yield ages of 2792−2751 Ma (Noce et al., 2005), and while the relationship between the Catarina Mendes formation and the Nova Lima Group is unknown, it is feasible that the younger zircon population represents the age of deposition.

Sample C03, the amphibolite dike, has just one zircon population at ca. 2760 Ma that is interpreted to be the crystallization age for the dike.

Sample V-1, the garnet bearing amphibolite, is interpreted to have a metamorphic age of ca. 2057 Ma for the amphibolite dike based on the morphology of the younger zircons (structureless or patchy zonation) as well as low Th/U ratios (<0.1). This coincides with the titanite age of the sample of 2040 Ma. The crystallization age of the dike is unresolvable because the remaining zircons gave a range of discordant ages between 2600−2300 Ma.

The titanite ages of D04, V-1 and MT3 are 2073 ± 7 Ma, 2043 ± 12 Ma and 2042 ± 11 Ma, respectively, and are interpreted to be metamorphic ages because titanite forms from the breakdown of rutile and ilmenite (Tanner and Evans, 2003). The closure temperature of titanite is estimated to be > 660−700 °C (depending on grain size; Scott and St-Onge, 1995; Bingen and van Breemen, 1998; Tanner and Evans, 2003), which is similar to the peak conditions obtained in this study. Furthermore, similar metamorphic ages have been obtained from syntectonic garnet in a dome-border shear zone which had an Sm−Nd age of 2095 ± 65 Ma (Marshak et al., 1997) and also monazite and titanite U−Pb ages obtained in the basement (Machado et al., 1992; Noce, 1995; Schrank and Machado, 1996a, b; Vlach et al., 2003; Aguilar et al., 2017). Sample V-1 is the only sample that presents similar zircon and titanite ages, 2057 Ma and 2043 Ma, respectively. Thus, it is logical that the metamorphic evolution recorded by sample V-1 unequivocally occurred at ca. 2050 Ma. Potentially, the slightly younger titanite is a result of the difference in closure temperature between zircon and titanite (>900 °C, Lee et al., 1997 vs. 660−700 °C, Tanner and Evans, 2003).

Despite the presence of titanite in mineral separates for samples D04, V-1 and MT3, titanite was only observed in thin section in sample D04. In this sample it occurs in several textural settings: 1) as large, euhedral grains (up to 3 cm in length; Fig. 10J), 2) finer-grained subhedral grains (up to 500 μm; Fig. 10K) that contain inclusions of matrix minerals, 3) euhedral grains with cores of ilmenite, and 4) fine (up to 100 μm), elongate grains, which are intergrown with chlorite or occur along cracks in amphibole (Fig. 10K). Types 2−4 are more abundant in regions of the thin section that display fine-grained, randomly oriented epidote. In situ geochronology was conducted on three grains (one type 1 and two of type 2) with all analyses producing the same age within error of 2059 ± 9 Ma (Fig. 10L). This would suggest that the metamorphism experienced by sample D04 occurred at ca. 2050 Ma similar to sample V-1. However, the peak conditions experienced by sample V-1 at ca. 2050 Ma are 650−700 °C (Figs. 7 and 11), which is in the range required to reset titanite ages. Aguilar et al. (2017) also dated titanite from the Bação dome. Their
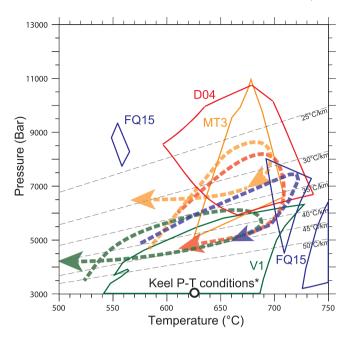
Figure 11. A compilation of the *P–T* paths experienced by the four investigated samples. The bold outlined fields indicate the interpreted peak assemblage of each sample. The dashed arrows indicate the interpreted *P–T* path for each sample. The spot indicates the *P–T* conditions obtained from a keel by Marshak et al. (1992).

sample FQ20 yielded a crystallization age of 2918 ± 10 Ma and a metamorphic age of ca. 2775 Ma (based on zircon dating by Lana et al., 2013), which is similar to the result here for sample MT3. Additionally, titanite had cores and dark colored domains that gave older ages of ca. 2690 Ma, whereas rims and patchy domains produced a mean age of ca. 2050 Ma. Aguilar et al. (2017) interpreted these two ages as the result of two distinct metamorphic histories.

Thus plausibly, sample D04 may have experienced two metamorphic events with the coarse-grained assemblage of amphibole and garnet forming at ca. 2700 Ma and a later event resetting the early titanite and forming the fine-grained assemblage (including the fine-grained titanite, which is texturally late). This would be consistent with textures observed in the thin sections. The titanite-bearing thin section contains only fragmented garnet that appears to be replaced by epidote, secondary amphibole and plagioclase suggesting that the process which resulted in titanite growth is also related to these fine-grained textures and post-dates garnet growth.

Sample FQ15 is the only sample that records two discrete metamorphic events (Fig. 11). The first produced a coarse-grained assemblage associated with leucosome formation, the second formed the fine-grained assemblage that occurs on the rims of clinopyroxene and hornblende grains, and included the growth of titanite. U–Pb zircon dating of grains from the leucosomes of this sample gave an age of 2728 ± 4 Ma (Farina et al., 2015b). This matches the age of metamorphic overgrowths on zircon crystals in banded gneisses from the same outcrop (2732 ± 10 Ma, sample FQ17, Farina et al., 2015a). Titanite from this sample yields an age of ca. 2050 Ma with some scattered older analyses (Aguilar, pers comm). Titanite from elsewhere in the Bação Complex gives ages of 2016–2080 Ma (Aguilar et al., 2017), which is similar to the ages obtained from the other samples in this study.

An age of ca. 2730 Ma for the coarse-grained assemblage may also explain the difference between the possible metamorphic zircon age in MT3 (of ca. 2775 Ma) and the titanite age (ca.

2040 Ma) with initial metamorphism producing the coarse mineral assemblage and metamorphic garnet with subsequent metamorphism at ca. 2066 Ma, which caused the resetting of the titanite age but not the zircon, and potentially also resulted in the higher X_{Ab} values recorded by plagioclase rims.

Thus, we interpret that the *P–T* evolution recorded by samples MT3, D04 and the earlier assemblage of FQ15 to have occurred at ca. 2775–2730 Ma, whereas the fine-grained assemblages in FQ15 and D04, and potentially also the *P–T* evolution of V-1, correspond to the metamorphic titanite ages of ca. 2050 Ma (Fig. 11).

8.2. Dome-and-keel formation

The two prevailing models for the formation of dome-and-keel provinces are partial convective overturn (Collins, 1989; Van Kranendonk et al., 2004, 2007, 2014) and core complex formation (Chemale and Rosière, 1993; Marshak et al., 1997; Holm et al., 1998; Kisters et al., 2003). The geology of the QF does not satisfy all the requirements for the partial convective overturn model at ca. 2050 Ma. Firstly, partial convective overturn would produce structures similar to diapirs with fabrics that wrap the domes and produce radial metamorphic lineations (Collins, 1989; Van Kranendonk et al., 2007). Such radial lineation patterns are not observed in the QF (Alkmim and Marshak, 1998). Furthermore, partial convective overturn requires a substantial amount of heat from syn-deformational magmatic rocks in order to soften and melt part of the crust prior to doming. For the QF, however, this process cannot be supported because of the age difference between TTG/Granitoid rocks (>2600 Ma; Lana et al., 2013; Romano et al., 2013; Farina et al., 2015a) and the ages recorded in the shear fabrics (2070–2050 Ma; this study) and the youngest sediments deposited in the keels (Minas Supergroup, ca. 2600–2100 Ma). U–Pb ages of some 15 samples from TTG and potassic granitoid have been published in the literature recently (Farina et al., 2015a). All U–Pb zircon ages (>2600 Ma) are at least 500 Ma older than the titanite ages (ca. 2050 Ma, this study), which record the timing of exhumation. If erosion had played a role in obscuring syn-doming magmatism, at least part of the crust would record evidence of injected dikes or feeders that would allow thermal softening and convective overturn. In contrast, the only basement rocks that were found to have experienced melting at ca. 2050 Ma occur in a shear zone south west of the QF. Migmatites from this shear zone give zircon U–Pb ages of ca. 2050–2030 Ma and are interpreted to record *P–T* conditions of ca. 730 °C and 5–6 kbar. These rocks are thought to have only experienced melting due to the presence of water in the shear zone (Carvalho et al., 2016, 2017). The surrounding basement rocks did not melt, neither were they overprinted by high enough temperatures to result in significant zircon recrystallization/resetting at ca. 2100 Ma. Sample V-1 of this study is the only sample from the Bação dome that was found to have metamorphic zircon at ca. 2050 Ma (c.f. this study, Lana et al., 2013; Romano et al., 2013; Farina et al., 2015a).

The metamorphic core complex model alone, is also inadequate to explain the formation of the QF dome-and-keel province. This is because metamorphic core complexes result from upwarping of shallow detachments overlain by a regional array of normal faults. This results in a dome with shallowly dipping borders, unlike classic dome-and-keel terrains including the QF, which have steep to inverted boundaries (Marshak et al., 1997).

The prevailing model for dome-and-keel formation in the QF of Marshak et al. (1997) suggests a hybrid between these two models with orogenic thickening at ca. 2100 Ma creating heat, followed by orogenic collapse and extension, which juxtaposed the hot, felsic granite-gneiss complexes with the cold, dense greenstones. This resulted in gravitational inversion and upwarping of the domes.
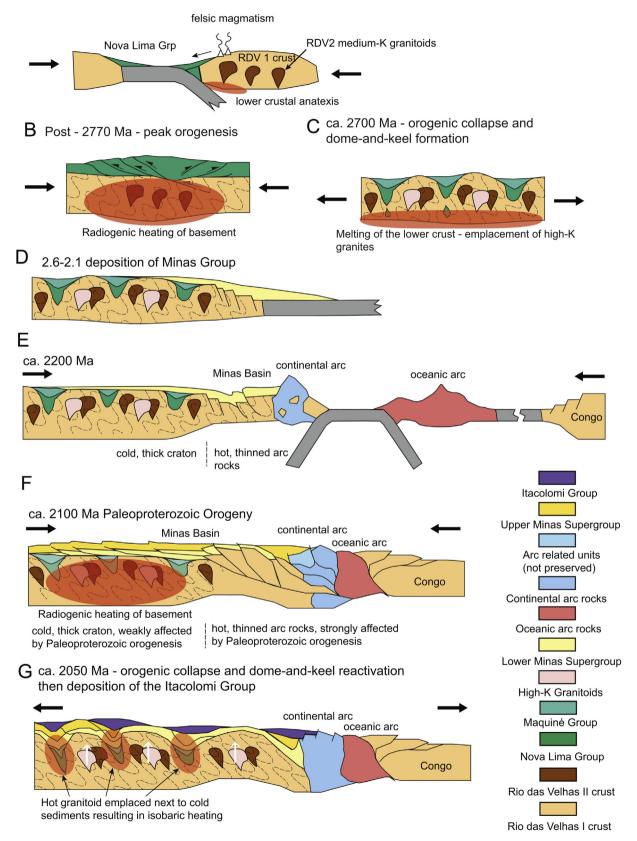
Figure 12. Tectonic model for the evolution of the QF based on the results of this study. Adapted from Aguilar et al. (2017). Parts A–G are referred to in the text.

Further extension caused the steepening of the dome borders and the current geology that is observed today.

8.3. Which model do the P–T results match?

The *P–T* results from this study are potentially compatible with the model of Marshak et al. (1997). However, the *P–T* evolution recorded by samples MT3, FQ15 and D04 occurred at ca. 2770–2730 Ma. Furthermore, at 2770–2700 Ma the QF had partially molten, buoyant TTG basement and the Nova Lima Group, a thick succession of mafic and volcaniclastic rocks. An age of ca. 2770 Ma is obtained across the QF for leucogranitic dikes, local migmatisation, and is commonly found as an age of metamorphic rims on igneous zircon (Lana et al., 2013; Farina et al., 2015a). It is additionally the age of two weakly foliated granite plutons (Caeté and Samambaia). Together, this suggests that the QF was affected by regional deformation and metamorphism at ca. 2770 Ma (Fig. 12).

Considering that the main elements required for partial convective overturn to occur were already in place at ca. 2770 Ma (Collins et al., 1998; Van Kranendonk et al., 2004, 2014), we suggest that the QF initially experienced orogenesis and crustal thickening, followed by extension and gravitational inversion at ca. 2770 Ma, producing the high-*P* and *T* metamorphism that is recorded in samples MT3, D04 and FQ15. The *P–T* paths of these samples are consistent with burial and heating followed by near isothermal decompression. The flat zoning in the garnet of sample D04 indicates peak temperature conditions were sustained for at least 20 million years (based on a radius of 500 μm and temperature of 700 °C; Carlson, 2006). This would be consistent with burial and heating of the TTGs, partial convective overturn resulting in upwarping of the TTG dome, and then cooling (Fig. 12A–C). In addition, the collision prior to dome-and-keel formation is consistent with the detrital zircon U–Pb age spectra of the Maquiné Group, which clearly sourced the TTG domes (Moreira et al., 2016, Fig. 12C).

The involvement of the Minas Supergroup in the keels suggests that the later crustal thickening during the 2100 Ma event again heated the basement enough to reset the titanite ages (this study, Aguilar et al., 2017) and reactivated the structures formed by the earlier dome-and-keel formation (Fig. 12D–G). This resulted in the Minas Supergroup keel rocks being juxtaposed against hot TTG causing the formation of a metamorphic aureole (i.e. Serra do Curral, Jordt-Evangelista et al., 1992) as well as the isobaric heating/cooling path that is recorded by sample V-1. This scenario would also explain the observation of Marshak et al. (1997) of the Minas keels crosscutting the Rio das Velhas keels.

The fine-grained assemblage of FQ15 records lower temperature, but higher pressure conditions of ca. 550 °C and 8–9 kbar. Plausibly the melting and dehydration of this rock made it unreactive to high temperature conditions but late metamorphic fluids allowed limited retrogression to occur, resulting in the lower temperature conditions that it preserves (Rubie, 1986; Carlson, 2010; Jamtveit and Austrhelm, 2010). Other studies have indicated the presence of cryptic secondary metamorphic events with a lack of significant recrystallization and renewed garnet growth during the later event, such as what is observed in samples FQ15, MT3 and D04 (see Young and Kylander-Clark, 2015; Dragovic et al., 2016 and references therein). The most common explanation is that the compositions of the investigated samples and the amount of fluid available during the second event are not amenable to further/new mineral growth (Young and Kylander-Clark, 2015; Dragovic et al., 2016).

This model for dome-and-keel formation in the QF is similar to that proposed for the eastern Pilbara dome-and-keel complex. Dome-and-keel formation here is suggested to be incremental, with episodes of partial convective overturn at 3320 Ma and 3240 Ma and later compressional events increasing the amplitude of the domes (Van Kranendonk et al., 2007). The initial dome-and-keel structures are proposed to have formed due to incubational heating with high heat producing TTGs (U = 2.5 ppm, Th = 11 ppm and K_2O = 2.5 wt.%; Bodorkos and Sandiford, 2006) being blanketed by a 15 km thick basalt succession. The build-up of radiogenic and mantle heat over time (ca. 100 M.y.) caused a decrease in viscosity of the underlying TTG crust and the density contrast between the TTGs and overlying greenstones resulted in partial convective overturn (Bodorkos and Sandiford, 2006).

The Bação dome has high radiogenic element contents (U 5.9 ppm, Th 17.3 ppm and K_2O 3.36 wt.%; Farina et al., 2015a) and the QF experienced significant magmatism at 2770–2700 Ma providing the heat needed for partial convective overturn.

The *P–T* conditions obtained for the Bação dome are also similar to what has been obtained from the eastern Pilbara dome-and-keel complex with metasediments from the edge of the Mount Edgar dome giving *P–T* conditions of 9–11 kbar and 450–550 °C and conditions of 6–7 kbar and 650–750 °C being obtained from the dome core (François et al., 2014).

Crustal thickening during 2100 Ma orogenesis likely resulted in radiogenic heating of the basement with orogenic collapse reactivating the earlier dome-and-keel formation structures.

The results of this study indicate that dome-and-keel formation occurred in the QF in the Archean. Gravitational inversion resulted from heating due to significant magmatism at this time. It is likely that the high-radiogenic element content of the Archean felsic crust, together with the high-density of typical Archean supracrustals is the reason that dome-and-keel provinces are a feature of Archean terrains (Bédard et al., 2013).

9. Conclusions

(1) The QF in the southern Sao Francisco Craton likely experienced two-stage dome-and-keel formation. Orogenesis and crustal thickening at 2770–2700 Ma resulted in peak metamorphic conditions of up to 8–9 kbar and 650–700 °C and a clockwise *P–T* path for rocks in the dome, with near isothermal decompression.

(2) Structures were reactivated at ca. 2050 Ma due to further burial during the 2100 Ma regional compressional event which resulted in crustal thickening, radiogenic heating of the basement and orogenic collapse. This reactivated the structures formed during the earlier dome-and-keel formation event, involved the younger Minas Supergroup within the keels and formed the metamorphic aureole.

(3) The formation of dome-and-keel provinces in Archean terrains is probably due to the inherent properties of Archean rocks, such as the high-radiogenic element contents in Archean felsic crust and the high-density of typical Archean supracrustals. These properties, combined with horizontal tectonic processes are responsible for dome-and-keel formation in the QF at ca. 2770 Ma.

Appendix A. Supplementary data

Supplementary data to this article can be found online at https://doi.org/10.1016/j.gsf.2019.02.009.

References

Aguilar, C., Alkmim, F.F., Lana, C., Farina, F., 2017. Palaeoproterozoic assembly of the São Francisco craton, SE Brazil: new insights from U-Pb titanite and monazite dating. Precambrian Research 289, 95–115. https://doi.org/10.1016/j.precamres.2016.12.001.

Albert, C., Farina, F., Lana, C., Stevens, G., Storey, C., Gerdes, A., Martínez Dopico, C., 2016. Archean crustal evolution in the Southern São Francisco craton, Brazil: constraints from U-Pb, Lu-Hf and O isotope analyses. Lithos 266–267, 64–86. https://doi.org/10.1016/j.lithos.2016.09.029.

Aleinikoff, J.N., Wintsch, R., Tollo, R.P., Unruh, D.M., Fanning, C.M., Schmitz, M.D., 2007. Age and origins of rocks of the Killingworth dome, south-central Connecticut: implications for the tectonic evolution of southern New England. American Journal of Science 307, 63–118. https://doi.org/10.2475/01.2007.04.

Alkmim, F.F., Marshak, S., 1998. The transamazonian orogeny in the Quadrilátero Ferrífero, Minas Gerais, Brazil: Paleoproterozoic collision and collapse in the southern São Francisco craton region. Precambrian Research 90, 29–58. https://doi.org/10.1016/S0301-9268(98)00032-1.

Alkmim, F.F., Martins-Neto, M.A., 2012. Proterozoic first-order sedimentary sequences of the São Francisco Craton, eastern Brazil. Marine and Petroleum Geology 33, 127–139. https://doi.org/10.1016/j.marpetgeo.2011.08.011.

Alkmim, F.F., Teixeira, W., 2017. The Paleoproterozoic mineiro belt and the Quadrilátero Ferrífero. In: Heilbron, M., Alkmim, F.F., Cordani, U.G. (Eds.), The São Francisco Craton and its Margins, Eastern Brazil, Geology Review Series. Springer-Verlag, pp. 71–94. https://doi.org/10.1007/978-3-319-01715-0_5.

Anhaeusser, C.R., Mason, R., Viljoen, M.J., Viljoen, R.P., 1969. Reappraisal of some aspects of Precambrian shield geology. Geological Society of America Bulletin 80, 2175–2200. https://doi.org/10.1130/0016-7606(1969)80[2175:AROSAO]2.0.CO;2.

Barbosa, J.S.F., Sabaté, P., 2004. Archean and Paleoproterozoic crust of the São Francisco craton, Bahia, Brazil: geodynamic features. Precambrian Research 133, 1–27. https://doi.org/10.1016/j.precamres.2004.03.001.

Bédard, J., Harris, L.B., Thurston, P.C., 2013. The hunting of the snArc. Precambrian Research 229, 20–48. https://doi.org/10.1016/j.precamres.2012.04.001.

Bickle, M.J., Bettenay, L.F., Boulter, C.A., Groves, D.I., Morant, P., 1980. Horizontal tectonic interaction of an Archaean gneiss belt and greenstones, Pilbara Block, Western Australia. Geology 8, 525–529. https://doi.org/10.1130/0091-7613(1980)8<525:HTIOAA>2.0.CO;2.

Bickle, M.J., Morant, P., Bettenay, L.F., Boulter, C.A., Blake, T.S., Groves, D.I., 1985. Archaean tectonics of the Shaw Batholith, Pilbara block, Western Australia: structural and metamorphic tests of the batholith concept. In: Ayers, L.D., Thurston, P.C., Card, K.D., Weber, W. (Eds.), Evolution of Archean Supracrustal Sequences, vol. 28. Geological Association of Canada, Special Paper, pp. 325–341.

Bingen, B., van Breemen, O., 1998. U-Pb monazite ages in amphibolite- to granulite-facies orthogneiss reflect hydrous mineral breakdown reactions: Sveconorwegian Province of SW Norway. Contributions to Mineralogy and Petrology 132, 336–353. https://doi.org/10.1007/s004100050428.

Bodorkos, S., Sandiford, M., 2006. Thermal and mechanical controls on the evolution of Archean crustal deformation: examples from Western Australia. In: Benn, K., Mareschal, J.-C., Condie, K.C. (Eds.), Archean Geodynamics and Environments, vol. 164. American Geophysical Union Geophysical Monograph, pp. 131–147. https://doi.org/10.1029/164GM10.

Brown, M., 2006. Duality of thermal regimes is the distinctive characteristic of plate tectonics since the Neoarchaean. Geology 34, 961–964. https://doi.org/10.1130/G22853A.1.

Brown, M., 2007a. Metamorphic conditions in orogenic belts: a record of secular change. International Geology Review 49, 193–234. https://doi.org/10.2747/0020-6814.49.3.193.

Brown, M., 2007b. Metamorphism, plate tectonics and the supercontinent cycle. Earth Science Frontiers 14, 1–18. https://doi.org/10.1016/S1872-5791(07)60001-3.

Brown, M., 2010. Paired metamorphic belts revisited. Gondwana Research 18, 46–59. https://doi.org/10.1016/j.gr.2009.11.004.

Brown, M., 2015. Paleo- to Mesoarchean polymetamorphism in the Barberton Granite-Greenstone Belt, South Africa: constraints from U-Pb monazite and Lu-

Hf garnet geochronology on the tectonic processes that shaped the belt: Discussion. Bulletin of the Geological Society of America 127, 1550–1557. https://doi.org/10.1130/B31198.1.

Carlson, W.D., 2006. Rates of Fe, Mg, Mn, and Ca diffusion in garnet. American Mineralogist 91, 1–11. https://doi.org/10.2138/am.2006.2043.

Carlson, W.D., 2010. Dependence of reaction kinetics on H2O activity as inferred from rates of intergranular diffusion of aluminium. Journal of Metamorphic Geology 28, 735–752. https://doi.org/10.1111/j.1525-1314.2010.00886.x.

Carvalho, B.B., Sawyer, E.W., Janasi, V.A., 2016. Crustal reworking in a shear zone: transformation of metagranite to migmatite. Journal of Metamorphic Geology 34, 237–264. https://doi.org/10.1111/jmg.12167.

Carvalho, B.B., Janasi, V.A., Sawyer, E.W., 2017. Evidence for Paleoproterozoic anataxis and crustal reworking of Archean crust in the São Francisco Craton, Brazil: a dating and isotopic study of the Kinawa migmatite. Precambrian Research 291, 98–118. https://doi.org/10.1016/j.precamres.2017.01.019.

Chemale Jr., F., Rosière, C.A., 1993. Arquitetura de domo e bacio no Quadrilátero Ferrífero no Proterozoic Inferior. Socidade Brasilera Geologia Boletim. Nucleo Minas Gerais 12, 172–175.

Chemale Jr., F., Rosière, C.A., Endo, I., 1994. The tectonic evolution of the Quadrilátero Ferrífero, Minas Gerais, Brazil. Precambrian Research 65, 25–54. https://doi.org/10.1016/0301-9268(94)90098-1.

Chen, S.F., Libby, J.W., Wyche, S., Riganti, A., 2004. Kinematic nature and origin of regional-scale ductile shear zones in the central Yilgarn Craton, Western Australia. Tectonophysics 394, 139–153. https://doi.org/10.1016/j.tecto.2004.08.001.

Chown, E.H., Harrap, R., Abdelali, M., 2002. The role of granitic intrusions in the evolution of the Abitibi belt, Canada. Precambrian Research 115, 291–310. https://doi.org/10.1016/S0301-9268(02)00013-X.

Clarke, G.L., Daczko, N.R., Nockolds, C., 2001. A method for applying matrix corrections to X-ray intensity maps using the Bence-Albee algorithm and Matlab. Journal of Metamorphic Geology 19, 635–644. https://doi.org/10.1046/j.0263-4929.2001.00336.x.

Coggon, R., Holland, T.J.B., 2002. Mixing properties of phengitic micas and revised garnet-phengite thermobarometers. Journal of Metamorphic Geology 20, 683–696. https://doi.org/10.1046/j.1525-1314.2002.00395.x.

Collins, W.J., 1989. Polydiapirism of the Archean Mount Edgar batholith, Pilbara block, Western Australia. Precambrian Research 43, 41–62. https://doi.org/10.1016/0301-9268(89)90004-1.

Collins, W.J., Van Kranendonk, M.J., Teyssier, C., 1998. Partial convective overturn of Archaean crust in the east Pilbara Craton, Western Australia: driving mechanisms and tectonic implications. Journal of Structural Geology 20, 1405–1424. https://doi.org/10.1016/S0191-8141(98)00073-X.

Condie, K.C., Pease, V. (Eds.), 2008. When Did Plate Tectonics Begin on Planet Earth?, vol. 440. Geological Society of America Special Paper, pp. 1–29.

Cutts, K.A., Stevens, G., Hoffmann, J.E., Buick, I.S., Frei, D., Münker, C., 2014. Paleo-mesoarchean polymetamorphism in the Barberton granite-greenstone belt, South Africa: constraints from U-Pb monazite and Lu-Hf garnet geochronology on the tectonicprocesses that shaped the belt. Bulletin of the Geological Society of America 126, 251–270. https://doi.org/10.1130/B30807.1.

Cutts, K.A., Stevens, G., Kisters, A., 2015. Reply to "Paleo- to Mesoarchean Polymetamorphism in theBarberton Granite-Greenstone Belt, South Africa: Constraints from U-Pb Monazite and Lu-Hf Garnet Geochronology on the Tectonic Processes that Shaped the Belt: Discussion" by M. Brown.Bulletin of the Geological Society of America, vol. 127, pp. 1558–1563. https://doi.org/10.1130/B31304.1.

Cutts, K.A., Lana, C., Alkmim, F., Peres, G., 2018. Metamorphic imprints on units of the southern Araçuaí Belt, SE Brazil: the history of superimposed Transamazonian and Brasiliano orogenesis. Gondwana Research 58, 211–234. https://doi.org/10.1016/j.gr.2018.02.016.

Davies, G.F., 1992. On the emergence of plate tectonics. Geology 20, 963–966. https://doi.org/10.1130/0091-7613(1992)020<0963:OTEOPT>2.3.CO.

De Capitani, C., Petrakakis, K., 2010. The computation of equilibrium assemblage diagrams with Theriak/Domino software. American Mineralogist 95, 1006–1016. https://doi.org/10.2138/am.2010.3354.

Diener, J.F.A., Powell, R., White, R.W., Holland, T.J.B., 2007. A new thermodynamic model for clino- and orthoamphiboles in the system Na_2O-CaO-FeO-MgO-Al_2O_3-SiO_2-H_2O-O. Journal of Metamorphic Geology 25, 631–656. https://doi.org/10.1111/j.1525-1314.2007.00720.x.

Dimroth, E., Imreh, L., Goulet, N., Rocheleau, M., 1983. Evolution of the south-central segment of the Archean Abitibi belt, Quebec. Part II: tectonic evolution and geomechanical model. Canadian Journal of Earth Sciences 20, 1355–1373. https://doi.org/10.1139/e83-124.

Dorr II., J.V.N., 1969. Physiographic, Stratigraphic and Structural Development of the Quadrilátero Ferrífero, Minas Gerais, Brazil, vol. 641-A. USGS/DNPM, Washington Professional Paper, p. 110.

Dragovic, B., Guevara, V.E., Caddick, M.J., Baxter, E.F., Kylander-Clark, A.R.C., 2016. A pulse of cryptic granulite-facies metamorphism in the Archean Wyoming Craton revealed by Sm-Nd garnet and U-Pb monazite geochronology. Precambrian Research 283, 24–49. https://doi.org/10.1016/j.precamres.2016.07.010.

Drake, A.A., Morgan, B.A., 1980. Precambrian Plate Tectonics in the Brazilian Shield – Evidence from the Pre-minas Rocks of the Quadrilátero Ferrífero, Minas Gerais, vol. 1119-B. USGS/DNPM, Washington Professional Paper, pp. 1–19.

Droop, G.T.R., 1987. A general equation for estimating Fe^{3+} concentrations in ferromagnesian silicates and oxides from microprobe analyses, using

stoichiometric criteria. Mineralogical Magazine 51, 431–435. https://doi.org/10.1180/minmag.1987.051.361.10.

Farina, F., Albert, C., Lana, C., 2015a. The Neoarchean transition between medium- and high-K granitoids: clues from the southern São Francisco craton (Brazil). Precambrian Research 266, 375–394. https://doi.org/10.1016/j.precamres.2015.05.038.

Farina, F., Cutts, K., Lana, C., 2015b. Cryptic evidence of fluid-present partial melting of Archean banded gneisses in the Southern São Francisco Craton (Brazil): Implications for the evolution of the continental crust. In: 8th Hutton Symposium on Granites and Related Rocks, Florianopolis, abstract volume, PT, p. 024.

Farina, F., Albert, C., Martinez Dopico, C., Aguilar Gil, C., Moreira, H., Hippertt, J., Cutts, K., Lana, C., Alkmim, F.F., 2016. The Archean-Paleoproterozoic evolution of the Quadrilátero Ferrífero (Brasil): current models and open questions. Journal of South American Earth Sciences 68, 4–21. https://doi.org/10.1016/j.jsames.2015.10.015.

François, C., Philippot, P., Rey, P., Rubatto, D., 2014. Burial and exhumation during Archean sagduction in the east Pilbara granite-greenstone terrane. Earth and Planetary Science Letters 396, 235–251. https://doi.org/10.1016/j.epsl.2014.04.025.

Gerdes, A., Zeh, A., 2006. Combined U-Pb and Hf isotopic LA-(MC-)ICP-MS analyses of detrital zircons: comparison with SHRIMP and new constraints for the provenance and age of an Armorican metasediment in Central Germany. Earth and Planetary Science Letters 249, 47–61. https://doi.org/10.1016/j.epsl.2006.06.039.

Gerya, T., 2014. Precambrian geodynamics: concepts and models. Gondwana Research 25, 442–463. https://doi.org/10.1016/j.gr.2012.11.008.

Green, E.C.R., Holland, T.J.B., Powell, R., 2007. An order-disorder model for omphacitic pyroxenes in the system jadeite-diopside-hedenbergite-acmite, with applications to eclogitic rocks. American Mineralogist 92, 1181–1189. https://doi.org/10.2138/am.2007.2401.

Hamilton, W.B., 1998. Archean magmatism and deformation were not products of plate tectonics. Precambrian Research 91, 143–179. https://doi.org/10.1016/S0301-9268(98)00042-4.

Hartmann, L.A., Endo, I., Suita, M.T.F., Santos, J.O.S., Frantz, J.C., Carneiro, M.A., Naughton, N.J., Barley, M.E., 2006. Provenance and age delimitation of Quadrilátero Ferrífero sandstones based on zircon U-Pb isotopes. Journal of South American Earth Sciences 20, 273–285. https://doi.org/10.1016/j.jsames.2005.07.015.

Heaman, L.M., 2009. The application of U–Pb geochronology to mafic, ultramafic and alkaline rocks: an evaluation of three mineral standards. Chemical Geology 261 (1–2), 42–51.

Heilbron, M., Cordani, U.G., Alkmim, F.F. (Eds.), 2017. TheSão Francisco Craton, Eastern Brazil. Tectonic Genealogy of a Miniature Continent. Regional Geology Reviews. Springer International Publishing Co., p. 331.

Herz, N., 1978. Metamorphic Rocks of the Quadrilátero Ferrífero, Minas Gerais, Brazil, vol. 641-C. USGS/DNPM, Washington Professional Paper, pp. 1–81.

Hickman, A., 1984. Archaean diapirism in the Pilbara block, western Australia. In: Kröner, A., Greiling, R. (Eds.), Precambrian Tectonics Illustrated. Schwei-zerbart'sche Verlagsbuchhandlung, Stuttgart, pp. 113–127.

Hippertt, J.F., 1994. Structures indicative of helicoidal flow in a migmatitic diaper (Bação Complex, southeastern Brazil). Tectonophysics 234, 169–196. https://doi.org/10.1016/0040-1951(94)90210-0.

Hippertt, J., Davis, B., 2000. Dome emplacement and formation of kilometer-scale synclines in a granite-greenstone terrain (Quadrilátero Ferrífero, southeastern Brazil). Precambrian Research 102, 99–121. https://doi.org/10.1016/S0301-9268(00)00061-9.

Holland, T.J.B., Powell, R., 1998. An internally consistent thermodynamic data set for phases of petrological interest. Journal of Metamorphic Geology 16, 309–343. https://doi.org/10.1111/j.1525-1314.1998.00140.x.

Holland, T.J.B., Powell, R., 2003. Activity-composition relations for phases in petrological calculations: an asymmetric multicomponent formulation. Contributions to Mineralogy and Petrology 145, 492–501. https://doi.org/10.1007/s00410-003-0464-z.

Holm, D., Schneider, D., Lux, D., 1998. Dome-and-keel provinces formed during Paleoproterozoic orogenic collapse − core complexes, diapirs, or neither?: examples from the Quadrilátero Ferrífero and the Penokean orogeny: comment and reply. Geology 26, 475–477. https://doi.org/10.1130/0091-7613(1998)026<0475:DAKPFD>2.3.CO;2.

Hudleston, P.J., Schultz-Ela, D., Southwick, D.L., 1988. Transpression in an Archean greenstone belt, northern Minnesota. Canadian Journal of Earth Sciences 25, 1060–1068. https://doi.org/10.1139/e88-103.

Jackson, S.E., Pearson, N.J., Griffin, W.L., Belousova, E.A., 2004. The application of laser ablation-inductively coupled plasma-mass spectrometry to in-situ U-Pb zircon geochronology. Chemical Geology 211, 47–69. https://doi.org/10.1016/j.chemgeo.2004.06.017.

Jamtveit, B., Austrhelm, H., 2010. Metamorphism: the role of fluids. Elements 6, 153–158. https://doi.org/10.2113/gselements.6.3.153.

Jordt-Evangelista, H., Alkmim, F.F., Marshak, S., 1992. Metamorfismo progressivo e a ocorrência de três polimorfos de de Al₂SiO₅ na formação Sabará, Ibirité, Quadrilátero Ferrífero, MG. Revista da Escola de Minas. Ouro Preto 45, 157–160.

Kelsey, D.E., 2008. On ultrahigh-temperature crustal metamorphism. Gondwana Research 13, 1–29. https://doi.org/10.1016/j.gr.2007.06.001.

Kinny, P.D., McNaughton, N.J., Fanning, C.M., Maas, R., 1994. 518 Ma Sphene (Titanite) from the Khan Pegmatite, Namibia, Southwest Africa: a potential ion-microprobe standard. In: Abstract Presented at the 8th International Conference on Geochronology, Cosmochronology and Isotope Geology, vol. 1107. USGS Circular, p. 171.

Kisters, A.F.M., Stevens, G., Dziggel, A., Armstrong, R.A., 2003. Extensional detachment faulting and core-complex formation in the southern Barberton granite-greenstone terrain, South Africa: evidence for a 3.2 Ga orogenic collapse. Precambrian Research 127, 355–378. https://doi.org/10.1016/j.precamres.2003.08.002.

Kretz, R., 1983. Symbols for rock-forming minerals. American Mineralogist 68, 277–279.

Lana, C., Tohver, E., Cawood, P., 2010a. Quantifying rates of dome-and-keel formation in the Barberton granitoid-greenstone belt, South Africa. Precambrian Research 177, 99–211. https://doi.org/10.1016/j.precamres.2009.12.001.

Lana, C., Kisters, A.F.M., Stevens, G., 2010b. Exhumation of Mesoarchean TTG gneisses from the middle crust: insights from the Steynsdorp core complex, Barbertongranitoid-greenstone terrain, South Africa. Geological Society of America Bulletin 122, 183–197. https://doi.org/10.1130/B26580.1.

Lana, C., Alkmim, F.F., Armstrong, R., Scholz, R., Romano, R., Nalini Jr., H.A., 2013. The ancestry and magmatic evolution of Archean TTG rocks of the Quadrilátero Ferrífero province, southeast Brazil. Precambrian Research 231, 157–173. https://doi.org/10.1016/j.precamres.2013.03.008.

Lee, J.K.W., Williams, I.S., Ellis, D.J., 1997. Pb, U and Th diffusion in natural zircon. Nature 390, 159–162. https://doi.org/10.1038/36554.

Lin, S., 2005. Synchronous vertical and horizontal tectonism in the Neoarchean: kinematic evidence from a synclinal keel in the northwestern Superior craton, Canada. Precambrian Research 139, 181–194. https://doi.org/10.1016/j.precamres.2005.07.001.

Lin, S., Parks, J., Heaman, L.M., Simonetti, A., Corkery, M.T., 2013. Diapirism and sagduction as a mechanism for deposition and burial of "Timiskaming-type" sedimentary sequences, Superior Province: evidence from detrital zircon geochronology and implications for the Borden Lake conglomerate in the exposed middle to lower crust in the Kapuskasing uplift. Precambrian Research 238, 148–157. https://doi.org/10.1016/j.precamres.2013.09.012.

Lima da Silva, S., 2005. Projeto APA Sul RMBH Estudos Do Meio Físico, Geologia V. 1. Belo Horizonte. CPRM, p. 70.

Ludwig, K.R., 2003. Isoplot/Ex Version 3.00: a Geochronological Toolkit for Microsoft Excel. Berkeley Geochronology Center, Berkeley, CA.

Machado, N., Carneiro, M.A., 1992. U-Pb evidence of the late Archean tectono-thermal activity in the southern São Francisco shield, Brazil. Canadian Journal of Earth Sciences 29, 2341–2346. https://doi.org/10.1139/e92-182.

Machado, N., Noce, C.M., Ladeira, E.A., de Oliveira, O.A.B., 1992. U-Pb geochronology of the Archean magmatism and Proterozoic metamorphism in the Quadrilátero Ferrífero, southern São Francisco craton, Brazil. Geological Society of America Bulletin 104, 1221–1227. https://doi.org/10.1130/0016-7606(1992)104<1221:UPGOAM>2.3.CO;2.

Machado, N., Schrank, A., Noce, C.M., Gauthier, G., 1996. Ages of detrital zircon from Archean-Paleoproterozoic sequences: implications for Greenstone Belt setting evolution of a Transamazonian foreland basin in Quadrilátero Ferrífero, southeast Brazil. Earth and Planetary Science Letters 141, 259–276. https://doi.org/10.1016/0012-821X(96)00054-4.

Mahar, E.M., Baker, J.M., Powell, R., Holland, T.J.B., Howell, N., 1997. The effect of Mn on mineral stability in metapelites. Journal of Metamorphic Geology 15, 223–238. https://doi.org/10.1111/j.1525-1314.1997.00011.x.

Marshak, S., Alkmim, F.F., Jordt-Evangelista, H., 1992. Proterozoic crustal extension and the generation of dome-and-keel structures in an Archaean granite−greenstone terrane. Nature 357, 491–493. https://doi.org/10.1038/357491a0.

Marshak, S., Tinkham, D., Alkmim, F.F., Brueckner, H., Bornhorst, T., 1997. Dome-and-keel provinces formed during Paleoproterozoic orogenic collapse - core complexes, diapirs, or neither?: examples from the Quadrilatero Ferrifero and the Penokean Orogen. Geology 25, 415–418. https://doi.org/10.1130/00917613(1997)025<0415:DAKPFD>2.3.CO;2.

Martínez Dopico, C.I., Lana, C., Moreira, H.S., Cassino, L.F., Alkmim, F.F., 2017. U-Pb ages and Hf-isotope data of detrital zircons from the late Neoarchean-Paleoproterozoic Minas Basin, SE Brazil. Precambrian Research 291, 143–161. https://doi.org/10.1016/j.precamres.2017.01.026.

Mattinson, J.M., 2010. Analysis of the relative decay constants of ²³⁵U and ²³⁸U by multi-step CA-TIMS measurements of closed-system natural zircon samples. Chemical Geology 275, 186–198. https://doi.org/10.1016/j.chemgeo.2010.05.007.

Mazdab, F.K., 2009. Characterization of flux-grown trace-element-doped titanite using high-mass-resolution ion microprobe (SHRIMP-RG). The Canadian Mineralogist 47, 813–831. https://doi.org/10.3749/canmin.47.4.813.

Möller, A., O'Brien, P.J., Kennedy, A., Kröner, A., 2003. Linking growth episodes of zircon and metamorphic textures to zircon chemistry: an example from the ultrahigh-temperature granulites of Rogaland (SW Norway). In: Vance, D., Müller, W., Villa, I.M. (Eds.), Geochronology: Linking the Isotopic Record with Petrology and Textures, vol. 220. Geological Society, London, Special Publication, pp. 65–81. https://doi.org/10.1144/GSL.SP.2003.220.01.04.

Moreira, H., Lana, C., Nalini, H.A., 2016. The detrital zircon record of an Archean convergent basin in the Southern São Francisco Craton, Brazil. Precambrian Research 275, 84–99. https://doi.org/10.1016/j.precamres.2015.12.015.

Moreira, H., Seixas, L., Storey, C., Fowler, M., Lasalle, S., Stevenson, R., Lana, C., 2018. Evolution of Siderian juvenile crust to rhyacian high Ba-Sr magmatism in the Mineiro belt, southern São Francisco craton. Geoscience Frontiers 9, 977–995. https://doi.org/10.1016/j.gsf.2018.01.009.

Morris, P.A., Witt, W.K., 1997. Geochemistry and tectonic setting of two contrasting Archaean felsic volcanic associations in the Eastern Goldfields, Western Australia. Precambrian Research 83, 83–107. https://doi.org/10.1016/S0301-9268(97)00006-5.

Mueller, W.U., Daigneault, R., Mortensen, J.K., Chown, E.H., 1996. In: Archean Terrane Docking: Upper Crust Collision Tectonics, Abitibi Greenstone Belt, vol. 265. Tectonophysics, Quebec, Canada, pp. 127–150. https://doi.org/10.1016/S0040-1951(96)00149-7.

Myers, J.S., Watkins, K.P., 1985. Origin of granite-greenstone patterns, Yilgarn block, western Australia. Geology 13, 778–780. https://doi.org/10.1130/0091-7613(1985)13<778:OOGPYB>2.0.CO;2.

Nelson, D.R., 1997. Evolution of the Archaean granite-greenstone terranes of the eastern goldfields, western Australia: SHRIMP U-Pb zircon constraints. Precambrian Research 83, 57–81. https://doi.org/10.1016/S0301-9268(97)00005-3.

Nijman, W., Kloppenburg, A., de Vries, S.T., 2017. Archaean basin margin geology and crustal evolution: an East Pilbara traverse. Journal of the Geological Society 174, 1090–1112. https://doi.org/10.1144/jgs2016-127.

Noce, C.M., 1995. Geocronologia dos eventos magmáticos, sedimentares e metamórficos na região do Quadrilátero Ferrífero, Minas Gerais (Unpublished PhD Thesis). Instituto de Geociências Universidade de São Paulo, São Paulo, p. 129.

Noce, C.M., Machado, N., Teixeira, W., 1998. U-Pb geochronology of gneisses and granitoids in the Quadrilátero Ferrífero (southern São Francisco craton): age constraints for Archean and Paleoproterozoic magmatism and metamorphism. Revista Brasileira de Geociencias 28, 95–102.

Noce, C.M., Zucchetti, M., Baltazar, O.F., Armstrong, R., Dantas, E.L., Renger, F.E., Lobato, L.M., 2005. Age of felsic volcanism and the role of ancient continental crust in the evolution of the Neoarchean Rio das Velhas greenstone belt (Quadrilátero Ferrífero, Brazil): U–Pb zircon dating of volcaniclastic gray-wackes. Precambrian Research 141, 67–82. https://doi.org/10.1016/j.precamres.2005.08.002.

Palin, R.M., Weller, O.M., Waters, D.J., Dyck, B., 2016. Quantifying geological uncertainty in metamorphic phase equilibria modelling; a Monte Carlo assessment and implications for tectonic interpretations. Geoscience Frontiers 7, 591–607.

Renger, F.E., Noce, C.M., Romano, A.W., Machado, N., 1995. Evolução sedimentar do Supergrupo Minas: 500 Ma. de registro geológico no Quadrilátero Ferrífero, Minas Gerais, Brasil. Geonomos 2, 1–11.

Romano, R., Lana, C., Alkmim, F.F., Stevens, G.S., Armstrong, R., 2013. Stabilization of the southern portion of the São Francisco Craton, SE Brazil, through a long-lived period of potassic magmatism. Precambrian Research 224, 143–159. https://doi.org/10.1016/j.precamres.2012.09.002.

Rubie, D.C., 1986. The catalysis of mineral reactions by water and restrictions on the presence of aqueous fluid during metamorphism. Mineralogical Magazine 50, 399–415. https://doi.org/10.1180/minmag.1986.050.357.05.

Sandiford, M., Van Kranendonk, M.J., Bodorkos, S., 2004. Conductive incubation and the origin of dome-and-keel structure in Archean granite-greenstone terrains: a model based on the eastern Pilbara Craton, Western Australia. Tectonics 23, TC1009. https://doi.org/10.1029/2002TC001452.

Schrank, A., Machado, N., 1996a. Idades U-Pb em monazitas e zircões das Minas deMorro Velho e Passagem de Mariana, Quadrilátero Ferrífero, MG. In: Anais 39thCongresso Brasileiro de Geologia, Salvador, vol. 6. Sociedade Brasileira de Geologia, pp. 470–472.

Schrank, A., Machado, N., 1996b. Idades U-Pb em monazitas e zircões do distritoaurífero de Caeté, da Mina de Cuiabá e do Depósito de Carrapato, QuadriláteroFerrífero (MG). In: Congresso Brasileiro de Geologia, Salvador. Sociedade Brasileira de Geologia, vol. 6, pp. 473–475.

Schrank, A., Souza Filho, C.R., Roig, H.L., 1990. Novas Observações sobre as Rochas Ultramáficas do Grupo Quebra Osso e Formação Córrego dos Boiadeiros, Greenstone Belt Rio Velhas − MG, vol. 1. Cadernos Instituto de Geociências/UNICAMP, pp. 6–29.

Scott, D.J., St-Onge, M.R., 1995. Constraints on Pb closure temperatures in titanite based on rocks from the Ungava orogen, Canada: implications for U-Pb geochronology and P-T-t path determinations. Geology 23, 1123–1126. https://doi.org/10.1130/0091-7613(1995)023<1123:COPCTI>2.3.CO;2.

Sizova, E., Gerya, T., Stüwe, K., Brown, M., 2015. Generation of felsic crust in the Archean: a geodynamic modeling perspective. Precambrian Research 271, 198–224. https://doi.org/10.1016/j.precamres.2015.10.005.

Sláma, J., Kosler, J., Condon, D.J., Crowley, J.L., Gerdes, A., Hanchar, J.M., Horstwood, M.S.A., Morris, G.A., Nasdala, L., Norberg, N., Schaltegger, U., Schoene, B., Tubrett, M.N., Whitehouse, M.J., 2008. Plešovice zircon − a new natural reference material for U-Pb and Hf isotopic microanalysis. Chemical Geology 249, 1–35. https://doi.org/10.1016/j.chemgeo.2007.11.005.

Stacey, J.S., Kramers, J.D., 1975. Approximation of terrestrial lead isotope evolution by a two-stage model. Earth and Planetary Science Letters 26, 207–221. https://doi.org/10.1016/0012-821X(75)90088-6.

Stern, R.J., 2005. Evidence from ophiolites, blueschists, and ultrahigh-pressure metamorphic terranes that the modern episode of subduction tectonics began in Neoproterozoic time. Geology 33, 557–560. https://doi.org/10.1130/G21365.1.

Stowell, H., Stein, E., 2005. The significance of plagioclase-dominant coronas on garnet, Wenatchee Block, Northern Cascades, Washington, USA. The Canadian Mineralogist 43, 367–385. https://doi.org/10.2113/gscanmin.43.1.367.

Tanner, P.W.G., Evans, J.A., 2003. Late Precambrian U-Pb titanite age for peak regional metamorphism and deformation (Knoydartian orogeny) in the western Moine, Scotland. Journal of the Geological Society (London) 160, 555–564. https://doi.org/10.1144/0016-764902-080.

Teixeira, W., Figueiredo, M.C.H., 1991. An outline of Early Proterozoic crustal evolution in the São Francisco Craton. Brazil: a review. Precambrian Research 53, 1–22. https://doi.org/10.1016/0301-9268(91)90003-S.

Teixeira, W., Caneiro, M.A., Noce, C.M., Machado, N., Sato, K., Taylor, P.N., 1996. Pb, Sr and Nd isotope constraints on the Archean evolution of gneissic-granitoid complexes in the southern São Francisco Craton, Brazil. Precambrian Research 78, 151–164. https://doi.org/10.1016/0301-9268(95)00075-5.

Teixeira, W., Oliveira, E.P., Marques, L.S., 2017. Nature and evolution of the Archean crust of the São Francisco craton. In: Heilbron, M., Cordani, U.G., Alkmim, F.F. (Eds.), São Francisco Craton, Eastern Brazil. Tectonic Genealogy of a Miniature Continent. Regional Geology Reviews. Springer International Publishing Co., pp. 29–56

Tindle, A.G., Webb, P.C., 1994. PROBE-AMPH a spreadsheet to classify microprobe-derived amphibole analyses. Computers and Geosciences 20, 1201–1228. https://doi.org/10.1016/0098-3004(94)90071-X.

Van Hunen, J., Moyen, J.F., 2012. Archean subduction: fact or fiction? Annual Review of Earth and Planetary Sciences 40, 195–221. https://doi.org/10.1146/annurev-earth-042711-105255.

Van Kranendonk, M.J., Collins, W.J., Hickman, A., Pawley, M.J., 2004. Critical tests of vertical vs. horizontal tectonic models for the Archaean East Pilbara granite-greenstone terrane, Pilbara Craton, Western Australia. Precambrian Research 131, 173–211. https://doi.org/10.1016/j.precamres.2003.12.015.

Van Kranendonk, M.J., Smithies, R.H., Hickman, A.H., Champion, D.C., 2007. Review: secular tectonic evolution of Archean continental crust: interplay between horizontal and vertical processes in the formation of the Pilbara Craton, Australia. Terra Nova 19, 1–38. https://doi.org/10.1111/j.1365-3121.2006.00723.x.

Van Kranendonk, M., Kroner, A., Hoffmann, J.E., Nagel, T.J., Anhaeusser, C., 2014. Just another drip: Re-analysis of a proposed mesoarchean suture from the Barberton mountain land, South Africa. Precambrian Research 254, 19–35. https://doi.org/10.1016/j.precamres.2014.07.022.

Vlach, S.R.F., Campos Neto, M.C., Caby, R., Basei, M.A.S., 2003. Contact metamorphism in metapelites from the Nova Lima Group, Rio das Velhas Supergroup, Quadrilátero Ferrífero: a monazite Th-U-Pb dating by the electron-probe microanalyser. In: IV South American Symposium on Isotope Geology, Salvador. Short Papers, vol. 1, pp. 307–310.

White, R.W., Powell, R., Clarke, G.L., 2002. The interpretation of reaction textures in Fe-rich metapelitic granulites of the Musgrave block, central Australia: constraints from mineral equilibria calculations in the system K_2O-FeO-MgO-Al_2O_3-SiO_2-H_2O-TiO_2-Fe_2O_3. Journal of Metamorphic Geology 20, 41–55. https://doi.org/10.1046/j.0263-4929.2001.00349.x.

White, R.W., Pomroy, N.E., Powell, R., 2005. An in situ metatexite-diatexite transition in upper amphibolite facies rocks from Broken Hill, Australia. Journal of Metamorphic Geology 23, 579–602. https://doi.org/10.1111/j.1525-1314.2005.00597.x.

White, R.W., Powell, R., Holland, T.J.B., 2007. Progress relating to calculation of partial melting equilibria for metapelites. Journal of Metamorphic Geology 25, 511–527. https://doi.org/10.1111/j.1525-1314.2007.00711.x.

Williams, I.S., Collins, W.J., 1990. Granite-greenstone terranes in the Pilbara Block, Australia, as coeval volcano-plutonic complexes; evidence from U-Pb zircon dating of the Mount Edgar Batholith. Earth and Planetary Science Letters 97, 41–53. https://doi.org/10.1016/0012-821X(90)90097-H.

Young, D.J., Kylander-Clark, A.R.C., 2015. Does continental crust transform during eclogite facies metamorphism? Journal of Metamorphic Geology 33, 331–357. https://doi.org/10.1111/jmg.12123.